Thesis for the Degree of Licentiate of Engineering

Vertical-Cavity Surface-Emitting Lasers with Facet-Etched Metasurfaces

Erik Strandberg

Photonics Laboratory
Department of Microtechnology and Nanoscience - MC2
Chalmers University of Technology
Göteborg, Sweden, 2024

Vertical-Cavity Surface-Emitting Lasers with
Facet-Etched Metasurfaces
Erik Strandberg
Göteborg, January 2024

Chalmers University of Technology
Microtechnology and Nanoscience - MC2
Photonics Laboratory
SE-412 96 Göteborg, Sweden
Phone: +46 (0) 31 772 1000

ISSN 1652-0769
Technical Report MC2-469

Printed in Sweden by Reproservice, Chalmers University of Technology
Göteborg, Sweden, December 2024

Vertical-Cavity Surface-Emitting Lasers with facet-etched Metasurfaces

Erik Strandberg
Photonics Laboratory - Department of Microtechnology and Nanoscience - Chalmers University of Technology

Abstract

The vertical-cavity surface-emitting laser (VCSEL) is a ubiquitous device today. It is responsible for efficiently powering the short-reach fiber-optic links in data centers and registering your face every time you unlock your iPhone. The VCSEL's popularity comes from its micro-sized cavity, enabling the laser to lase with low threshold currents, inherent single longitudinal mode, and excellent high-speed modulation performance. However, the small cavity size implies that the emitted beam will have a significant divergence. Which means that the VCSEL needs to be packaged together with bulky external optics to perform even the simplest optical task. One of the more recent advancements in nanophotonics is called metasurfaces, a surface patterned with nanoparticles that can tailor the phase and polarization state for an incident beam. By carefully designing the geometry of the nanoparticles, it is possible to replicate and combine the output of essentially any classical refractive optical element, all in an optical component with a thickness that is of the same order as the wavelength of the beam.

The idea behind this work is to monolithically integrate metasurfaces directly in the facet of the VCSEL, removing the need for any beam shaping optics and delivering an arbitrary beam while maintaining the small footprint of the laser diode. In this thesis, I present how to design and fabricate a VCSEL with an integrated metasurface and how we have utilized them to construct miniaturized illumination modules for biophotonics. We have demonstrated an unconventional metasurface design that can very efficiently, $> 90\%$, deflect light to large angles, $> 60^\circ$ and circumvents the inherent problem of aspect-ratio dependent etching associated with monolithic integration. The VCSELs with facet-etched metasurfaces have enabled a combined dark-field and total internal reflection microscope module, and a surface-plasmon resonance sensing module with comparable to the state-of-the-art resolution at $\Delta n = 4.9 \cdot 10^{-6}$ refractive index units.

Keywords: vertical-cavity surface-emitting lasers, metasurfaces, metagratings, miniaturized biophotonics, surface plasmon resonance

Publications

This thesis is based on the work contained in the following papers:

[A] Mindaugas Juodėnas, **Erik Strandberg**, Alexander Grabowski, Johan Gustavsson, Hana Jungová-Šipová, and Mikael Käll. "*High-angle deflection of metagrating-integrated laser emission for high-contrast microscopy*", in *Light: Science and Applications*, 12.1 (2023): 251.
doi: 10.1038/s41377-023-01286-0

[B] **Erik Strandberg**, Mindaugas Juodėnas, Hana Jungová-Šipová, and Mikael Käll. "*Flat Plasmonic Biosensor with an On-Chip Metagrating-Integrated Laser*", Submitted.

Contents

Acknowledgment

First and foremost, I would like to extend my biggest possible thank you to Åsa, both for introducing me to the photonics lab, VCSELs, for support, guiding words, and encouragement along the way for the last three years. Mikael for inviting me to be around bio nanophotonics and for a great general excitement about nanophotonics. Thank you, Anders for a smooth introduction to the Ph.D. journey and all the clean room duties, and thank you, Philippe for making sense of electromagnetic theory. Beyond the professors, an extra large special thank you to Mindaugas, for supplying this project with nanofabrication expertise, and for making the bio imaging lab thoroughly enjoyable to be in; I will not ponder on what I would have done without you. Alexander for all the guidance in the clean room, the introduction to chess, and the steady supply of internet content. Thank you, Hana for all biophotonics and pipette guidance. To the other final Ph.D. student of the optoelectronic lab, Hans, thank you for spare snus and for managing to even make the tropical heat in Shenzen enjoyable. Thank you to Lars for all discussions about how optics actually work and the chess games, and to Timo for making my last thesis writing during Covid less lonely. Thank you to Niclas for all the electron beam lithography support and for the unprecedented amount of joy you bring to nanofabrication. I had the great pleasure to guide a handful of student projects in the optoelectronic lab, Isac, Christoffer, Sofia, Jacob, Theodor, and Gustav, thank you for supplying the lab with extra excitement; I wish you all the best with future endeavors. Thank you, Tintin for some great nanofabrication and laughs. Thank you to the GaN group for adopting me. Of course, a huge thank you to everyone

else working in the photonics lab, bio nanophotonics department, and the myfab clean room, no one mentioned, no one forgotten. Thank you to Simon, Per, Frida, and Erika for making the first five years of the physics education bearable and thank you to my mother and brother, Sophia and David, for making the first eighteen years of my life bearable. The final thank you is saved for my star and the love of my life, Hanna, without you everything is gray.

Erik Strandberg
Göteborg, December 2024

Acronyms

ARDE	Aspect-Ratio Dependent Etching
CCD	Charge-Coupled Device
DF	Dark-Field
DBR	Distributed Bragg Reflector
EBL	Electron-beam Lithography
EEL	Edge-Emitting Laser
GaAs	Gallium Arsenide
HDMS	Hexamethyldisilazane
MQW	Multiple Quantum Well
NA	Numerical Aperture
OSA	Optical Spectrum Analyzer
PDMS	Polydimethylsiloxane
QW	Quantum Well
RIE-ICP	Inductively Coupled Plasma Reactive Ion Etch
SEM	Scanning Electron Microscope
SMSR	Side-Mode Suppression Ratio
SPP	Surface Plasmon Polariton
SPR	Surface Plasmon Resonance
TIR	Total Internal Reflection
TLM	Transfer Length Method
VCSEL	Vertical-Cavity Surface-emitting Laser

CHAPTER 1

Introduction

1.1 Background

Since the first demonstration of the laser, by stimulated emissions from a ruby crystal in 1960 [1], it has arguably been one of the most transformative devices for modern society and all fields of the natural sciences. Since then, it has been an exciting quest for the laser community to find new materials that can induce lasing, delivering new lasers at different wavelengths and with different strengths. For example, using a high-voltage electric current to excite molecules in C_2O for cutting and welding metals [2], optically pumping Nd:YAG crystals for optical surgery and the detection of gravitational waves [3], or utilizing relativistic electrons to create extreme ultraviolet light in complex material science [4].

One of the more common types of laser today is the semiconductor laser [5], where the band gap of a semiconductor crystal is utilized to emit light. Since the band gap is dependent on crystal constituents and their ratio [6], it is possible to achieve emission ranging from the UV into the far-infrared. The wide band gap of the AlGaN material system can produce UV wavelengths, 210-320 nm [7, 8], InGaN-AlGaN supports emission over the visible wavelength, for example, 405 nm laser diode used in high-density optical storage disks, spotlights and headlights [9, 10]. For longer wavelengths in the visible spectrum InGaAlP-

GaAs takes over, with for example 650 nm diodes used in old DVD players [11,12], InGaAsP-InP can emit in the far-infrared covering the wavelength spectrum used in optical communication 1310-1550 nm [13, 14], and the narrow separation in energy between sub-bands is used in quantum cascade lasers to emit light into the far-infrared as far as 24 μm [15]. Finally, for emission in deep red into the near-infrared, 750-1100 nm, AlGaAs is the material of choice and used for pumping the mentioned Nd:YAG lasers [16, 17] and pumping erbium-doped fiber amplifiers [18]. The AlGaAs system has been especially attractive for laser diodes, since AlAs and GaAs are lattice matched; it enables epitaxial growth of layers with a high refractive index contrast. AlGaAs can be highly doped, both p- and n-type, to produce low-resistance ohmic contacts, and since the epitaxial growth of AlGaAs is very mature, the produced wafers have a very low defect density [19–21]. All of the different material systems pose their own challenges for producing a stable laser diode, and research is still devoted to finding suitable ways to produce electrically pumped devices for each material system, and for incorporating new fabrication and new growing techniques [22]. The current and future interest in the semiconductor laser can be attributed to nanofabrication, an field that has seen huge investments, research, and improvements following the undeniable success of the transistor, allowing the semiconductor laser to piggyback on the development of new and improved techniques.

The two main types of semiconductor lasers are the edge-emitting laser (EEL) and the vertical-cavity surface-emitting laser (VCSEL). The main difference, as their names suggest, is the direction of emission from the substrate. The gallium arsenide (GaAs) VCSEL with emission in the infrared has since the inception in 1979 [23] and commercialization in 1996 been the laser of choice for short-reach fiber-optic links in data centers [24,25], short-range 3D sensing applications [26], and used to be the light source in an optical computer mouse [27]. Due to their micro-sized cavity, the VCSEL has an extremely compact footprint, low threshold current for lasing, excellent high-speed performance at low power, and inherent single longitudinal mode emission. In addition, the VCSEL emits a circular symmetric beam from the surface of the semiconductor wafer, in contrast to the EEL, which enables screening during the fabrication and in turn leads to higher fabrication yields of mounted lasers. However, though EEL and VCSELs can be made extremely compact and energy efficient, their small cavity sizes imply that the emitted beam

will always have a significant divergence. Which requires the lasers to be packaged together with bulky external optics to perform even the simplest tasks; optics such as shaping the laser beam to suit the application.

One of the more recent revolutionary developments in nanophotonics is the dielectric optical metasurfaces, the latest development in the miniaturization of beam shaping optical elements. The miniaturization first started with Fresnel, who realized that the ordinary lens focuses light by introducing a laterally varying phase accumulation from the curved geometry of the lens surface. Since light is an electromagnetic wave, it is periodic by 2π and Fresnel understood that he only needed to be able to control a phase shift up to 2π to focus a beam. This realization led to the construction of the Fresnel lens, where the curved surface of the lens only achieves a phase accumulation of between $0-2\pi$ and the rest of the glass is removed [28], reducing the weight of the lens. It is still possible to see Fresnel lenses in a university classroom that uses an overhead projector or in your nearest lighthouse [29]. The next step in miniaturization is called diffractive optics and was made possible by nanofabrication techniques allowing fabrication of nanostructures with a comparable size to the wavelength of light [30,31]. In diffractive optics, a discrete pattern of different heights is structured to induce the laterally varying phase delay of 2π needed for beam shaping. Even though diffractive optics can create complex optical beam shaping [32], it faces several problems, foremost the complex nanofabrication process needed to etch a sub-wavelength pattern to several different discrete heights, needed for advanced beam shaping.

The dielectric metasurface is essentially an integrated diffractive optical element, but instead of varying the height to induce a phase delay, the geometry of discrete nanoparticles in a sub-wavelength lattice, called metaatoms, is utilized [33, 34], allowing for the entire optical element to be fabricated in one step. By tailoring the geometry of the metaatom, the metasurface can perform tasks that the diffractive optic cannot, such as extensive control over the polarization state [35, 36]. Moreover, the metasurface [37] can produce the optical output of essentially any classical refractive or diffractive optical element, such as lenses [38,39], blazed gratings [40], changing the polarization state [41], or any combination thereof [42], and the metasurface can even outperform classical optics in certain applications, such as single lenses with near-unity numerical

apertures [43]. So, the dielectric metasurface delivers any optical function from an optical element, from a surface of a single layer of dielectric metaatoms, with a thickness on the order of the wavelength of the beam, leading to an unparalleled reduction in the weight and size of any optical setup. This might all sound too good to be true; unfortunately, the metaatoms' geometry comes with resonances, which means that they have a relatively narrow wavelength band, compared to refractive optics, for which the wanted optical output is produced. It is currently a large quest to find the best solution to solve wide-band operation of metasurfaces [44]. Beyond the narrow band of operation, the fabrication of metasurfaces is usually relying on sub-wavelength lithography with electron beam lithography (EBL) which is very expensive, but alternatives to EBL are emerging such as nanoimprinting or self-assembled metasurfaces [45, 46]. Finally, optical metasurfaces can be structured into materials that can be externally tuned, which would allow for wavelength-thin active optical beam shaping, among others, electrically tunable transparent indium tin oxide [47], thermal tuning of resonant silicon disks [48], or infiltration of liquid crystal in resonant cavities [49].

1.2 Motivation

The VCSEL is the perfect candidate for monolithic integration of the metasurface directly on the facet of the laser. A GaAs-VCSEL can be grown on an undoped GaAs substrate, a dielectric material with very low defect density, which causes minimal scattering losses, and a high refractive index, which simplifies the fabrication because it reduces the needed etch depth for a dielectric metasurface. Furthermore, the VCSEL is inherently lasing with a single-mode longitudinal mode which is ideal for the, in general, narrow band operation of a dielectric metasurface. Finally, the laser diode's surface emission means that the metasurface can easily be etched directly into the facet of the laser. The metasurface removes the need for packaging the VCSEL with external optics; it becomes possible to fabricate laser diodes that produce an arbitrary beam directly from the chip, retaining the small footprint of the VCSEL. In addition, the laser diodes are fabricated on centimeter-sized chips with hundreds to thousands of individually addressable lasers, each of which can have its own dedicated metasurface. This creates the possibility to have chips emitting a plethora of different beams that each can be

designed to complete their own optical tasks and switched between extremely rapidly, which has limitless potential for miniaturized optical devices.

1.3 State-of-the-art

There are several demonstrations of different approaches to the integration of dielectric optical metasurfaces together with a semiconductor laser. The first two aimed to generate on-chip beams with orbital angular momentum by patterning a SiN_x metasurface on the facet of the VCSEL [50], and a SiN_x metasurface on a half-cavity VCSEL to induce orbital angular momentum [51]. The first demonstration of a monolithically integrated metasurface with a VCSEL was in 2020, where they collimated, deflected, and produced Bessel beams on-chip with dynamic phase metasurfaces [52]. The same group published an additional paper with dynamic phase metasurfaces with an extensive demonstration of array beams with different properties, large-angle deflection, and holography [53]. In 2022, they extended their fabrication to include what is called spin-decoupled metasurfaces, a combination of dynamic and geometric phase metasurfaces, and demonstrated holographic images of different polarizations and vortex beams [54]. Finally, a last demonstration with spin-decoupled metasurfaces was used to create several holograms with different polarizations from the same laser [55]. Beyond Genevet's group, there has also been a demonstration of integrated amorphous-Si metasurfaces on the facet of a VCSEL to create circularly polarized light, and by reverse biasing the diode, they demonstrated how it can be utilized as a photodetector for light with a circular polarization [56], and a demonstration of GaAs metasurface integrated in the top distributed Bragg reflector that both provides the needed reflectance for lasing and alters the polarization state of the emitted beam from linear to circular [57].

1.4 In this thesis

In this thesis, I present how bottom-emitting GaAs VCSELs, emitting light at 980 nm, with monolithically integrated optical metasurfaces, have been designed and fabricated. We have fabricated a diffractive-type metasurface, called a metagrating, that is able, through an unconven-

tional design, to collimate, in one dimension, and to deflect, in the other dimension, the emitted beam from the VCSEL, creating a fan-shaped beam directly from the laser chip. This laser is then used to perform miniaturized biophotonics. The first demonstration in Paper **A** [58] is a miniaturized illumination module for dark-field and total internal reflection (TIR) microscopy, two standard illumination techniques that deliver a large signal-to-noise ratio, since the background from the source is suppressed. Since the emitted beam is at a steep angle, the illuminated body is spatially offset from the illumination module; thus, it can be directly attached to an existing bright-field microscope, making it attractive as an affordable add-on for any existing microscope setup that needs extra functionalities. In addition, two neighboring VCSELs on the same chip provide the illumination needed for the dark-field and the TIR, which enables rapid switching between the two modes of microscopy of the same target. The second demonstration, in Paper **B**, uses the same type of metasurface design to excite surface plasmon polaritons (SPPs) in a thin metal film, which can be used to perform a biosensing technique called surface plasmon resonance (SPR). The illumination module is bonded to a glass slide that can be interfaced with a sensing slide that has both the metal film needed to support SPP excitation and bonded polydimethylsiloxane (PDMS) microfluidic channels for easy analyte perfusion. The full biosensor has been extensively characterized, and we demonstrate a comparable performance to the state-of-the-art SPR sensor, but with a miniaturized illumination and a not-seen-before flat form factor.

1.4.1 Thesis outline

The second chapter describes the lasing action of a semiconductor laser and how to design the VCSEL cavity for single-mode and single-polarization emission, as well as the fabrication process and the achieved performance of the laser diodes. In the third chapter, the principles of conventional phase-gradient and diffractive metasurfaces are introduced, and how to design and fabricate metasurfaces in GaAs. For the final chapter, the used design to realize the miniaturized illumination modules is described, and the two applications for the papers are briefly discussed.

CHAPTER 2

Vertical-Cavity Surface-Emitting Lasers

As the name suggests, the vertical-cavity surface-emitting laser (VCSEL) emits light normal to the surface of the semiconductor wafer. The cavity is formed by sandwiching a gain medium between two highly reflecting distributed Bragg reflectors (DBRs). The VCSEL is sometimes referred to as a micro-cavity laser and gains significant advantages from the small-sized cavity, such as low threshold currents and outstanding high-speed performance at low power consumption. The VCSELs fabricated for metasurface integration are substrate-emitting and designed to be lasing in a single longitudinal and transverse mode, and with pinned polarization over the entire biasing range of the VCSEL.

2.1 Laser fundamentals

Laser is an acronym for **L**ight **A**mplification by **S**timulated **E**mission of **R**adiation. The light emitted by stimulated emission is highly coherent and almost monochromatic, making the laser the ideal candidate for any application that demands a precise light source. To obtain stimulated emission as the dominant radiative process, three ingredients are required: a medium which can be pumped with energy to create optical gain, an energy pump for said medium, and a resonator to create a high energy density of photons at a certain wavelength [5, 59].

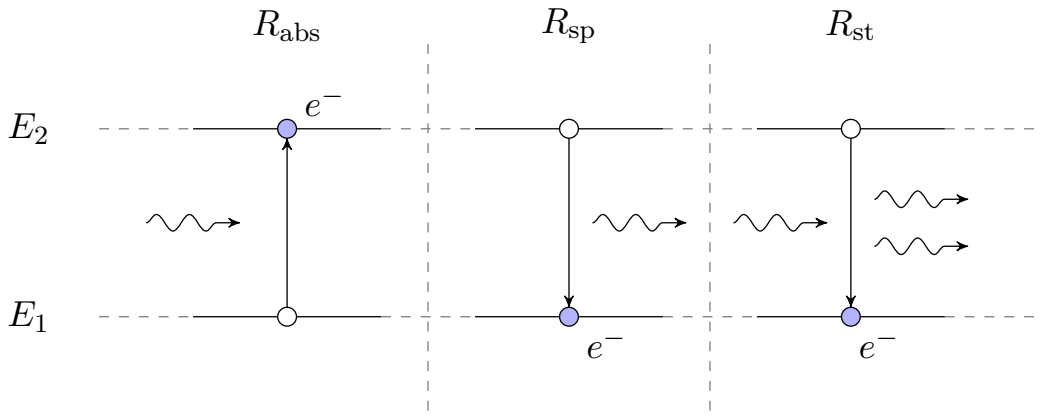

Figure 2.1: The three possible photon-electron processes of the two-level system. The incident and emitted photons all have a wavelength, $\lambda = hc/\Delta E$, corresponding to the energy difference of the two-level system.

2.1.1 Population inversion

Stimulated emission is a quantum interaction and to understand how to make it the dominant radiative process in a medium, it is instrumental to study one of the simpler quantum systems - the two-level system. In the two-level system, electrons can be in a low-, E_1, or high-energy state, E_2, the number of electrons per unit volume, populating these energy levels, is denoted by N_1 and N_2 respectively. In this system, there are three different one-electron-one-photon interactions that can take place, as shown in Fig. 2.1, between an electron in either state and a photon with a wavelength that corresponds to the separation of the energy levels,

$$\Delta E = E_2 - E_1 = \frac{hc}{\lambda} \quad \rightarrow \quad \lambda = \frac{hc}{\Delta E}, \tag{2.1}$$

where h is Planck's constant, c is the speed of light and λ the wavelength of the photon. In the first interaction, an electron can be excited from the lower-energy state to the higher-energy state, absorbing the photon in the process. The rate of absorption will be dependent on the density of electrons in the lower energy state and the energy density of the photons

$$R_{\text{abs}} = B_{12} N_1 \rho(\lambda), \tag{2.2}$$

where $\rho(\lambda)$ is the photon energy per unit volume between λ and $\lambda + d\lambda$. B_{12} is known as Einstein's B coefficient and is a function of the energy separation in the two-level system. For the second interaction, an electron in the higher-energy state can spontaneously be deexcited to the lower state, which produces a photon with wavelength λ, and

is known as spontaneous emission. The spontaneous emission does not need a photon to induce the interaction and is only dependent on the number of electrons in the higher energy level,

$$R_{\text{sp}} = A_{21} N_2, \tag{2.3}$$

where A_{21} is, again, Einstein's A coefficient. Finally, a photon can interact with an electron in the high-energy state and deexcite the electron. This interaction is called stimulated emission and produces an additional photon from the energy difference by the deexcitation of the electron. The rate of stimulated emission is therefore dependent on the electrons in the higher energy state and the energy density of photons in the gain medium,

$$R_{\text{st}} = B_{21} N_2 \rho(\lambda), \tag{2.4}$$

where B_{21} is, again, Einstein's B coefficient.

So, of the one-electron-one-photon interaction, there are two radiative processes that can generate light. Both are dependent on the number of electrons in the higher energy state, N_2. In thermal equilibrium, the number of electrons in the excited state is low, which makes absorption, R_{abs}, the dominant process of the two-level system. So, the first step to constructing a laser is to inject the gain medium with energy to excite electrons to the higher-energy state, where the excess of charge carriers induces non-equilibrium conditions; what is known as population inversion, that enables the generation of light.

2.1.2 Optical feedback

However, there are still two radiative processes, spontaneous, R_{sp}, and stimulated emission, R_{st}, and there is a key difference between the photons emitted from the two processes. Since the spontaneously emitted photons are from electrons deexciting from the conduction band by random fluctuations, they will be emitted with a random phase and wavelength. Thus, the radiation from spontaneous emission is isotropic and incoherent. On the other hand, the deexcitation of the electron in stimulated emission is induced by the incident photon, creating a quantum mechanical copy of the incident photon with exactly the same phase and wavenumber, giving rise to highly directional and coherent radiation.

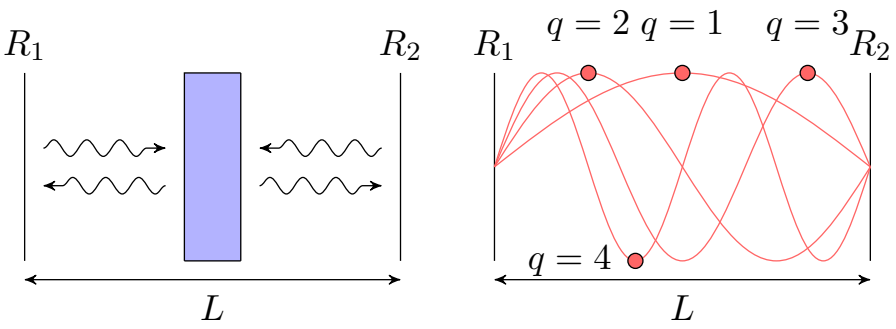

Figure 2.2: The Fabry-Perot cavity with two planar mirrors, with reflectance R_1 and R_2 respectively, separated by length L. The gain medium that can generate light by population inversion is sandwiched between the mirrors. The wavelength that fulfills Eq. 2.8 will form standing waves inside the cavity and resonate.

Unfortunately, the ratio between the rates of stimulated to spontaneous emission, under thermal equilibrium, can be found as,

$$R = \frac{R_{\text{st}}}{R_{\text{sp}}} = \frac{1}{e^{hc/\lambda k_B T} - 1}, \tag{2.5}$$

where k_B is the Boltzmann constant and T is the ambient temperature. At room temperature and at a wavelength $\lambda \ll k_B T$, the rate of spontaneous emission far exceeds the rate of stimulated emission. For example, at room temperature, $T = 300$ K with photons in the near infrared spectrum, $\lambda = 980$ nm, the ratio between the two processes is $R \approx 5 \cdot 10^{-24}$.

Fortunately, the rate of stimulated emission is dependent on another term as well; the energy density of photons, $\rho(\lambda)$, from Eq. 2.4. By placing the gain medium inside an optical resonator, it is possible to increase the photon density for a resonating wavelength and have stimulated emission dominating over the spontaneous. Again, it is instrumental to study the simplest possible resonator, the Fabry-Pérot resonator, as shown in Fig. 2.2, only consisting of two plane mirrors, with reflectance R_1 and R_2. The plane wave solution for the electric field propagating in the cavity along the z-axis can be written as,

$$\mathbf{E}(x, y, z) = \mathbf{E}_t(x, y) e^{-ikz} e^{\Gamma(g-\alpha)\frac{z}{2}}, \tag{2.6}$$

where $\mathbf{E}_t$ is the transverse electric field profile, $k = 2\pi n_{\text{neff}}/\lambda$ is the propagation constant along the z-axis, g and α are the gain and loss coefficients for propagation one round trip in the cavity, and Γ is the

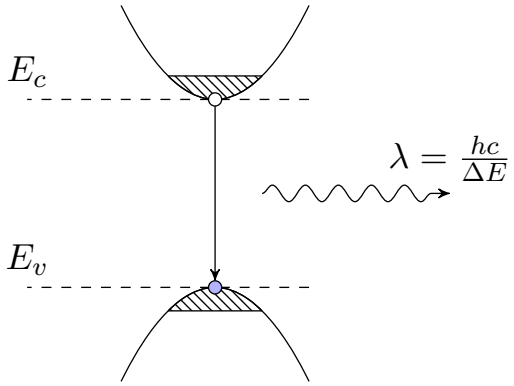

Figure 2.3: The direct band gap of the GaAs semiconductor crystal.

confinement factor that takes into account how much of the field is overlapping with the gain medium. The resonances of the cavity can be found by requiring that the field reproduces itself after propagating one round trip, $2L$, in the cavity,

$$\mathbf{E}(x,y,z) = \mathbf{E}(x,y,z+2L) \quad \rightarrow \quad 1 = \underbrace{e^{-2ikL}}_{\text{Phase}} \underbrace{\sqrt{R_1 R_2} e^{\Gamma(g-\alpha)}}_{\text{Amplitude}}. \tag{2.7}$$

The two terms of the result can be separated into two conditions for lasing. First the phase condition,

$$1 = e^{-2ikL} \quad \rightarrow \quad 2kL = 2\pi q \quad \rightarrow \quad \lambda = \frac{2Ln_{\text{neff}}}{q}, \tag{2.8}$$

where n_{neff} is the effective refractive index of the mode and q is the mode number. This gives the longitudinal resonating modes of the cavity. The first four modes for the Fabry-Perot cavity are shown in Fig. 2.2. The second term is referred to as the gain condition,

$$1 = \sqrt{R_1 R_2} e^{\Gamma(g-\alpha)L} \quad \rightarrow \quad g_{\text{th}} = \frac{1}{\Gamma}\left(\alpha + \frac{1}{2L}\ln\frac{1}{R_1 R_2}\right), \tag{2.9}$$

where g_{th} is known as the threshold material gain. g_{th} is the needed gain for the active region to perfectly balance the loss from propagation in the cavity and the loss from the mirror facets. When $g > g_{\text{th}}$ one photon will generate more than one photon per round trip in the cavity, creating a self-oscillating system where the energy density of the photons, $\rho(\lambda)$, can grow large, which increases the stimulated emission process, R_{st}, making the dominating process for generating light, creating coherent emission.

2.2 The semiconductor laser

Semiconductor lasers, or laser diodes, are emitters where stimulated emission is generated by injecting current or photons into a semiconductor crystal. The two main types are the edge-emitting laser (EEL), with a cavity along the length of the substrate, and the vertical-cavity surface-emitting laser (VCSEL), with a cavity vertical to the surface of the substrate. The active region, or gain medium, consists of a semiconductor crystal that has a direct band gap, where population inversion can be established in a forward-biased pn-junction, by injecting either photons or electrons. In Fig. 2.3 a direct band gap of semiconductor crystal, with a parabolic approximation for the conduction and valence band, is presented; the emitted photon will have a wavelength corresponding to the energy difference of the deexcitation, $\lambda = hc/\Delta E$. The resonant cavity, for optical feedback, is formed by reflection from the refractive index difference between different compositions of semiconductor materials, dielectric materials, and the index contrast to air.

2.2.1 The vertical-cavity surface-emitting laser

As mentioned, the VCSEL has a vertically oriented cavity. The fabricated VCSEL for this work is in the AlGaAs material system designed to lase at 980 nm. With the vertical cavity, the small optical confinement to the active region gives a very limited amount of gain from one round trip in the cavity, in comparison to the EEL, which creates a need for highly reflective mirrors to induce lasing. Usually, the VCSEL cavity has an effective length of one or several wavelengths, which makes the VCSEL inherently lasing with a single longitudinal mode. In Fig. 2.4**A** a top view of a fabricated GaAs bottom-emitting VCSEL, next to a cross-section of the VCSEL in Fig. 2.4**B**.

Quantum wells

Semiconductor lasers usually take advantage of thin layers of gain material, with a thickness on the order of $\approx$ 10 nm, called a quantum well (QW), where the discretization of the electron wavefunction in one dimension significantly alters the material properties [60]. The small volume of active material that needs to be pumped implies that only a small current is needed to achieve population inversion, which reduces the threshold current, even though it reduces the optical confinement.

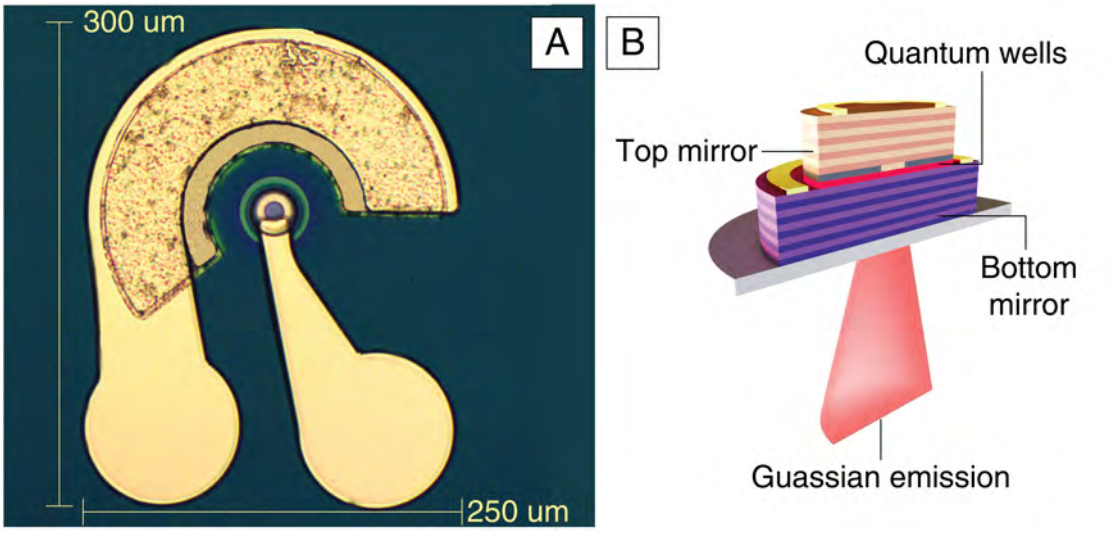

Figure 2.4: (**A**) Microscope image of a fabricated bottom-emitting GaAs-VCSEL. Note that most of the image is the probe pads for the laser. (**B**) A 3d render of the cross-section of the bottom-emitting GaAs-VCSEL.

The QW also has a reduced density of states compared to bulk material, which for a certain excess of carriers has a narrower gain spectrum, i.e. the wavelength range over which the active region can provide gain, at the band edge [61]. This, in turn, leads to a further decrease in threshold current, since population inversion at the band edge can be reached for lower excess current densities. Finally, the small thickness of the QW allows for strain engineering of the gain medium; the active layers can be grown with strain without exceeding the critical thickness where the material would crack, which enables further tailoring of the band structure [62].

The full active region usually consists of multiple quantum wells (MQWs), separated by barriers of some higher band gap material. The gain spectrum for GaAs is usually on the order of 10-100 nm, which red-shifts when biased. There is research dedicated to investigating QW with different compositions, called chirped QW, to enable more temperature-stable operation of the VCSEL [63]. Recently, it was demonstrated that it is possible to cascade several active regions of MQW, separated by tunnel junctions that can recycle carriers, to further increase the gain of the laser cavity [64].

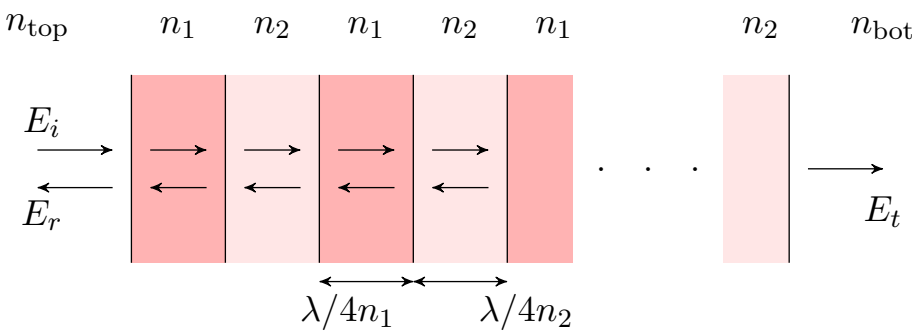

Figure 2.5: Illustration of a DBR with alternating layer with a higher, n_1, and lower, n_2 refractive index. If the layers have a thickness $\lambda/4n$ the transmitted field, E_t, experiences destructive interference and a mirror of arbitrary high reflectance, for a certain wavelength range, can be constructed.

Longitudinal modes

The short cavity gives rise to a large free spectral range between the longitudinal modes, i.e. a large gap in wavelength between the modes. The free spectral range can be calculated by taking the derivative of the mode number, q, with respect to the wavelength in the phase condition, Eq. 2.8, and is

$$\Delta\lambda = \frac{\lambda^2}{2Ln_{\text{g,eff}}}, \tag{2.10}$$

where $n_{\text{g,eff}} = 1 - \frac{\lambda}{n_{\text{eff}}}\frac{dn_{\text{eff}}}{d\lambda}$ is the effective group index of the mode. For a GaAs VCSEL with emission at $\lambda = 980$ and a one wavelength long cavity, the free spectral range is $\Delta\lambda \approx 140$ nm. This is much larger than the gain spectrum of the MQW; thus, the short cavity VCSEL inherently has one resonant longitudinal mode that can lase. However, the resonant wavelength is a function of the effective refractive index, Eq. n_{eff}, of the cavity, as seen from 2.8, which is also temperature-dependent. The refractive index of semiconductor materials usually increases with temperature, causing the resonant wavelength to red-shift with an increase in bias current.

Distributed Bragg reflectors

Since the optical confinement to the active region with the vertical cavity is very limited, the amount of generated photons from each round-trip is small, which in turn sets a very high requirement on the reflectance of the mirrors. The reflectance required to fabricate a lasing VCSEL is

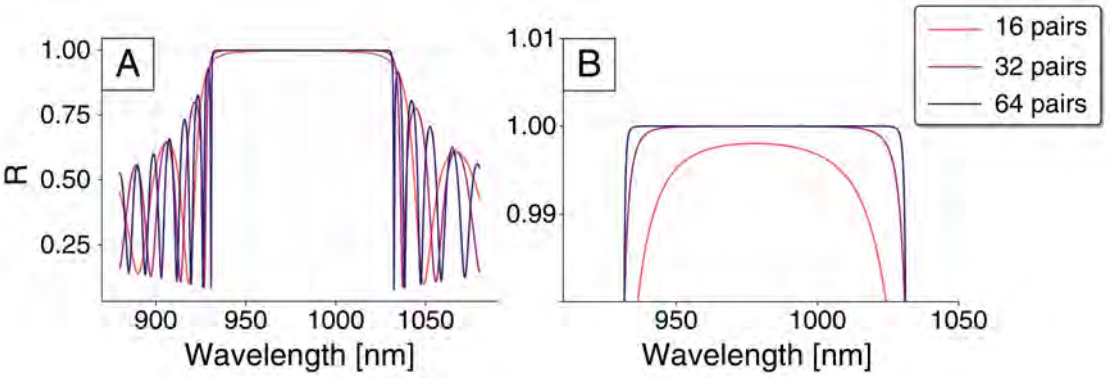

Figure 2.6: The reflectance from a DBR that is designed to highly reflect light at $\lambda = 980$ nm. (**A**) The reflectance from three different GaAs-AlAs DBR with 16, 32 and 64 mirror pairs. (**B**) Zoomed in image of the stopband where the reflectivity approaches unity and the the bandwidth of the stopband increases with the number of pairs in the DBR.

usually $R > 99\%$, which makes it necessary to employ DBRs, illustrated in Fig. 2.5. By alternating refractive index materials of a higher, n_1, and lower, n_1, refractive index, it is possible to create near-unity reflectance within a certain wavelength range.

When an incident beam, E_i, is illuminating the top of a DBR, there will be reflections from all the interfaces. If the thickness of each layer is exactly a quarter wavelength, the phase shift from each reflection back to the top is exactly $2\pi m$, where m is an integer. This means that all reflections will constructively interfere for the reflected field, E_r, and suppress the transmitted wave, E_t, by destructive interference. The reflectance from a DBR can be analyzed via the transfer matrix method [65] where the reflectance for a certain wavelength is found as,

$$R_{\mathrm{DBR}} = \left[\frac{n_{\mathrm{top}} - n_{\mathrm{bot}} \left(\frac{n_1}{n_2} \right)^{2N}}{n_{\mathrm{top}} + n_{\mathrm{bot}} \left(\frac{n_1}{n_2} \right)^{2N}} \right]^2 , \tag{2.11}$$

where n_1/n_2 is the refractive index contrast of the alternating layers in the stack, N is the number of mirror pairs, and n_{top}, n_{bot} are the refractive indices at the top and bottom of the stack respectively. From Eq. 2.11 the reflectivity of the DBR stack increases with the number of mirror pairs, N, and approaches unity. The spectral width of the stopband, the range of wavelength with high reflectivity, is determined by the index contrast, n_1/n_2, in the DBR, where a large contrast leads to

a wider stopband.

A huge benefit for the fabrication of a VCSEL in the AlGaAs material system is that GaAs and AlAs are lattice matched, making it possible to epitaxially grow many layer pairs of GaAs/AlAs, enabling the growth of very precise thicknesses with a relatively high index contrast, n_1/n_2, which gives a broad stop band around a chosen wavelength. In Fig. 2.6 the simulated reflectance spectrum of AlAs/GaAs DBR can be seen with three different amounts of mirror pairs, N. However, since the refractive index is, again, temperature dependent, the stop band of the DBR red-shifts in a GaAs-VCSEL. To successfully design a lasing VCSEL, is therefore a wavelength matching problem between the gain spectrum, the longitudinal resonating mode, and the reflectance spectrum of the DBR, all three of which have their own wavelength drift with respect to temperature. There have been demonstrations of temperature-stable VCSELs in GaN by utilizing materials with a negative thermo-optic coefficient to construct the DBR [66].

Oxide aperture

The DBR confines the optical field in the longitudinal direction. Furthermore, the charge carriers and photons need to be confined in the transverse direction [67]. The first VCSEL just consisted of an etched air post mesa, where the refractive index step from the semiconductor crystal to air provides the waveguiding structure. However, this design suffers greatly from high thermal resistance because of the surrounding air, and large scattering losses from rough etched sidewalls. Additionally, it is hard to place large enough contacts on top of the mesa for low resistance, while at the same time keeping the absorption losses low. The first commercial VCSEL developed a concept where protons are implanted deep into the top DBR [68]. The implanted protons passivated the semiconductor, forming an insulating layer, and can guide carriers through the center of the device. However, the proton implantation only takes care of the electrical confinement. In the proton implanted VCSEL, they only used the fact that as the laser heats up during operation, the heat creates a refractive index gradient, referred to as thermal lensing [69]. This is a suboptimal solution since the modal properties become strongly bias-dependent. Furthermore, since the protons need to be implanted deep within the mesa, the protons were prone to scattering and spreading out during the implantation, which made it very

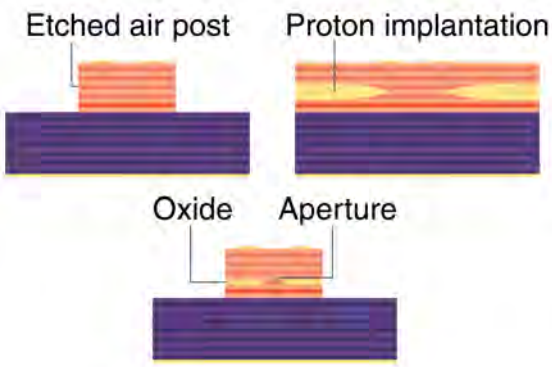

Figure 2.7: The three of the most prominent transverse mode control schemes for VCSELs.

difficult to precisely control and fabricate very small-aperture devices for single-mode lasing. The different aperture schemes are presented in Fig. 2.7.

The most popular solution for today's GaAs-VCSELs is the oxide aperture [70], where one or several layers in the p-doped top DBR have a significantly higher Al content [71, 72]. By oxidizing the VCSEL mesa during the fabrication, exposed surfaces will start forming into an oxide. But since the oxidation rate is a strong function of the aluminum content of each layer, it is possible to selectively oxidize certain layers with a large aluminum content [73]. The oxide aperture elegantly solves both the electron and photon confinement in one fabrication step [74]. The formed oxide has a higher resistance than the non-oxidized material, which confines electrons, and the oxide has a lower refractive index, which creates the waveguide structure for photon confinement.

The waveguide formation can be analyzed with effective index methods [75], which show that the modification of refractive index changes the local resonating wavelength, λ_0, as

$$\frac{\Delta n_{\text{eff}}}{n_{\text{eff}}} \approx \frac{\Delta \lambda_0}{\lambda_0}, \tag{2.12}$$

where the n_{eff} is the effective index of the VCSEL before oxidation. The waveguide structure that is formed by oxidation can be seen in Fig. 2.8**A**. By solving the wave equation from Maxwell's equations for a cylinder with the different effective indices as boundary conditions, as shown in

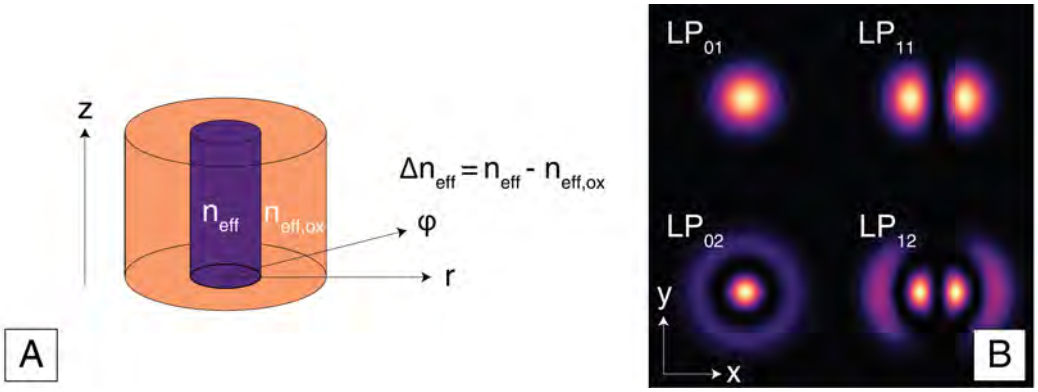

Figure 2.8: (**A**) The refractive indices of the oxide confined VCSEL. The oxidized layer creates lower effective refractive index in the cladding layer, $n_{\text{eff,ox}}$, compared to the core, n_{eff}. The refractive index difference creates a waveguide that is responsible for the transverse mode control of the VCSEL. (**B**) The first four LP modes of the VCSEL.

Fig. 2.8, the intensity of the transverse modes are [65]

$$I_{LP}(r,\phi) \propto |E_{LP}(r,\phi)|^2 = \left(\frac{2r^2}{\omega_0}\right)^2 \left[L_{p-1}^{(l)}\left(\frac{2r^2}{\omega_0}\right)\right] \begin{Bmatrix}\cos^2(l\phi)\\ \sin^2(l\phi)\end{Bmatrix} e^{-\frac{2r^2}{\omega_0}}, \tag{2.13}$$

where E_{LP} is the optical field strength, ω_0 is the $1/e^2$ radius of the mode, L_{p-1}^{l} is the l^{th} generalized Laguerre polynomial of order $p-1$, and ϕ is the azimuthal angle. These modes are referred to as the linearly polarized modes, LP. When l is larger than one, $l > 0$, the cos and sin factors represent the existence of orthogonal states rotated by $90°/l$ from each other. The eigenvalue when solving for the LP modes corresponds to the wavelength of the different modes

$$\lambda_{LP} = \lambda_0 \left[1 - (2p + l - 1)\sqrt{\frac{\Delta n_{\text{eff}}}{2\pi}}\frac{\lambda}{n_{\text{neff}} d_{\text{ox}}}\right], \tag{2.14}$$

where n_{eff} is the refractive index of the core of the waveguide. The fundamental LP_{01} has the longest wavelength with the higher-orders decreasing in wavelength. The diameter of the oxide aperture, d_{ox}, is the most significant parameter to control during the fabrication of the VCSEL, since it both controls the distribution of the transverse modes and the threshold current. The size of d_{ox} sets the extent of the waveguide which decides the transverse modes that it can support. The waveguided modes experience lower losses and will be able to lase. Since it is possible to tune the amount of losses the higher order modes experience, it

is possible to suppress the lasing of all higher order transverse modes. However, light is always generated for all the transverse modes within the gain spectrum, but a VCSEL is termed quasi-single mode laser when the side-mode suppression ratio (SMSR) is larger than 30 dB, meaning that the fundamental mode is lasing with 1000 times more intensity than any other of the higher order modes.

Since the oxide aperture also sets the transverse confinement of electrons, it also decides the active volume that needs to be pumped with carriers to induce lasing, setting the threshold current of the laser. However, since a small aperture will limit the area for current to pass through the laser, it will increase the total resistance of the laser, which increases the thermal build-up from ohmic heating. This implies that the VCSEL will reach thermal rollover earlier, limiting the maximum output power of the laser diode. The fabricated VCSELs in this thesis only have one layer in the top DBR with high aluminum content that is placed in an antinode of the optical field, to have the smallest possible refractive index step, Δn_{eff}, and is referred to as weakly guided VCSEL. The oxide aperture decides the modal distribution of the VCSEL; the higher order modes have a larger radial extent, as seen in Fig. 2.8**B**. The weak guiding allows for the largest radial distribution of the transverse mode, which means that the higher-order modes will be suppressed for the largest possible oxide aperture, allowing a high maximum output power in single-mode operation.

Furthermore, there is one more degree of freedom for the LP modes from Eq. 2.13. The electric field can also oscillate in two orthogonal polarizations perpendicular to the propagation direction. Therefore, the fundamental LP_{01} has two polarization states, and higher order modes with $l > 0$ have four different polarization states. The GaAs crystal is isotropic, meaning that the two orthogonal modes should have exactly the same wavelength. However, because of defects from growth or induced anisotropy from fabrication, the two modes generally have slightly different wavelengths, but this difference is usually not seen in a spectrum characterization of a VCSEL due to the limited resolution of spectrum meters used in standard laboratories, < 0.2 nm.

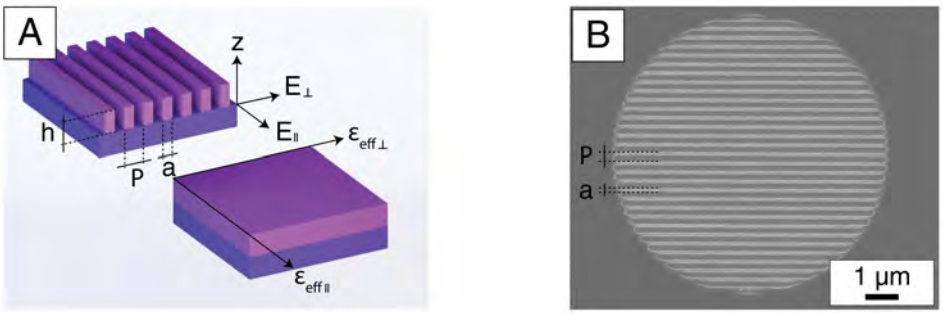

Figure 2.9: (**A**) The sub-wavelength grating can be approximated by an effective index medium with an anisotropic permitivitty for the electric field, depending on if the field is parallel with or orthogonal to the grating lines. (**B**) SEM image of the sub-wavelength grating etched into the top of the VCSEL substrate.

Polarization properties

It is desirable, especially for metasurface integration, to have the VCSEL emit light with a specific polarization with as much power as possible; research has been devoted to find possible modifications to the VCSEL that cause the polarization to be pinned down. The idea is to introduce some asymmetry in the VCSEL to either separate the two orthogonal states in wavelength or introduce higher losses for one of the polarization states. The standard modification for the top-emitting VCSEL is to etch a sub-wavelength surface grating [76, 77]. The grating lines create an anisotropic effective permittivity in the top mirror for an electric field that is polarized in the parallel or perpendicular direction compared to the grating bars,

$$\begin{aligned} \epsilon_{\text{eff},||} &= 1 + d\,(\epsilon - 1)\,, \\ \epsilon_{\text{eff},\perp} &= \frac{\epsilon}{d + \epsilon\,(1-d)}, \end{aligned} \tag{2.15}$$

where ϵ is the permittivity of the material in the grating lines and d is the duty cycle, as shown in Fig. 2.9**A** [78]. This effective permittivity approximation is valid as long as the period of the grating is small compared to the wavelength. Since the reflectance of the DBR is built up from destructive interference by reflections at interfaces between layers with $\lambda/4$ thickness, the modification of the permittivity can selectively decrease the reflectance for the different polarizations of the electric field. This in turn increases the losses for the lasing modes, enabling the laser

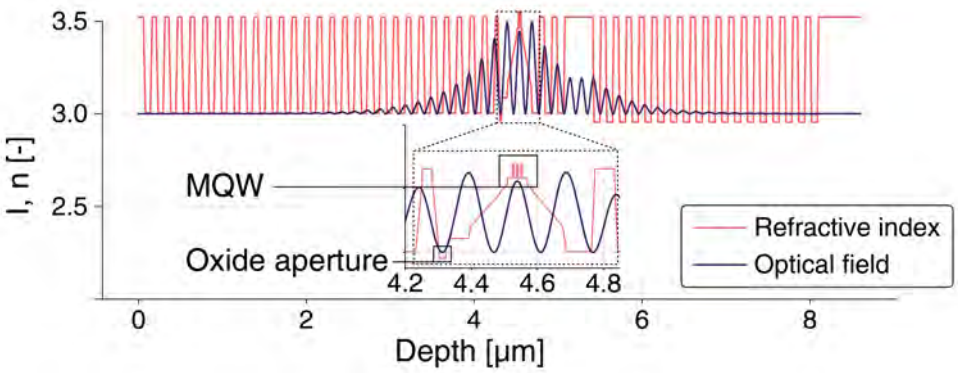

Figure 2.10: Refractive index profile and the fundamental resonating longitudinal mode of the cavity. The inset shows that the optical intensity has a maximum exactly centered on MQW for highest optical confinement and that is has a minimum centered on the oxide aperture for the weak guiding.

to only lase with one polarization over a larger range of bias currents. In Fig. 2.9**B** an scanning electron microscope (SEM) image of the sub-wavelength grating in the top mirror of the bottom-emitting VCSEL is presented.

However, the sub-wavelength grating has only been shown to work properly for the top-emitting VCSEL. Since the top DBR has a lower reflectance for outcoupling in the top-emitting VCSEL, there is still significant intensity at the top surface of the top mirror where the grating is incorporated. Which allows for the etching of a shallow grating, < 100 nm, in the top mirror to pin the polarization. For the bottom-side emitting VCSEL, with a highly reflective top mirror, there is almost no intensity that feels the refractive index difference from such a shallow top side grating. For the bottom-side emitting devices, the main technique explored to pin the polarization has been the etching of deep trenches next to the VCSEL mesa to induce an anisotropic relaxation of the active region, but the technique has not been able to demonstrate reliable performance [79, 80].

2.2.2 VCSEL cavity simulations - effective index method

The resonating modes of the VCSEL structure can be simulated with the effective index method [81]. The simulations performed here are, so-called, cold cavity simulations where only the electric field inside the cavity is considered. The gain in the active region is simulated by introducing an imaginary part of the refractive index of the MQW. In the

effective index method, the wave equation of the electric field is solved by assuming that the time dependence is harmonic with angular frequency ω, and can be discretized on a grid along the z-axis, labeled with i, into concentric circular slices as

$$E(r, z, \phi, t) = \eta_i E(r, \phi, t) e^{j\omega t}, \tag{2.16}$$

where η_i is the amplitude of the electric field in each region i. By also assuming that the envelope of the electric field is slowly varying, $\frac{\mathrm{d}^2 E}{\mathrm{d}t^2} \approx 0$, the above equation can be rearranged into an eigenvalue problem with the form

$$\frac{\mathrm{d}^2 \eta_i}{\mathrm{d}z^2} + k_0^2 \left(1 - \xi_i\right) \epsilon_i \eta_i = 0, \tag{2.17}$$

where ξ_i is the eigenvalue and ϵ_i is the corresponding permittivity in each region i. The name of the method comes from Eq. 2.17, where it can be seen that the eigenvalue for the solution represents the slight modification, $(1 - \xi_i)$, of the actual index into an effective index that is felt by the resonating mode. The full optical field of the bottom-emitting VCSEL and refractive index profile can be seen in Fig. 2.10. Since the solved eigenvalue in general is complex-valued, the imaginary part corresponds to the losses of the mode and thus it is possible to estimate the threshold gain, Eq. 2.9, as the amount of gain needed to be added to the MQW to compensate for the total losses of the longitudinal mode,

$$g_{\mathrm{th}} = \frac{k_0 \mathrm{Im}\left[\xi_i\right] \mathrm{Re}\left[\langle \epsilon_i \rangle\right]}{n_{\mathrm{QW}} u_i}, \tag{2.18}$$

where $\langle \epsilon_i \rangle$ is the weighted average effective index, n_{QW} is the refractive index of the quantum wells, and u_i is a binary function that is one in the i regions that make up the quantum wells and zero everywhere else. Besides threshold gain, it is also possible to estimate the quality factor for the cavity and the slope efficiency of the fabricated VCSEL.

2.2.3 VCSEL fabrication

The epitaxial structure designed with the effective index method, from the previous section, was for this work grown by Jenoptik AG using metal-organic chemical vapor deposition. A labeled cross-section of the final fabricated device can be seen in Fig. 2.11. The fabrication consists of depositing metal contacts to the p- and n-doped DBR for ohmic contact, etching down the VCSEL mesa, and selectively wet-oxidizing the

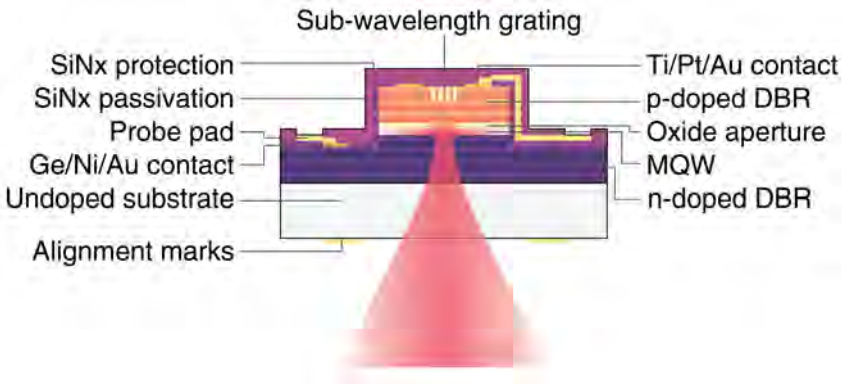

Figure 2.11: Labeled cross section of the fabricated GaAs VCSEL.

mesa to form the aperture. The top and the bottom sides of the chips are referred to as the VCSEL and metasurface sides, respectively. The final step, described in the next chapter, is to fabricate the optical metasurface; thus, it is of the highest importance to keep the metasurface side of the chip as pristine as possible during the entire fabrication run.

Process flow

The steps for the nanofabrication of a polarization-pinned bottom-emitting VCSEL suitable for monolithic integration of a metasurface are briefly described below.

1. Alignment marks

The first step is to pattern both the VCSEL and metasurface side with alignment marks for the rest of the fabrication process. The alignment marks are deposited by evaporation and consist of a metal stack with 20/50/100 nm of Ti/Pt/Au, respectively. Alignment marks are needed on both sides to precisely align the VCSEL to the metasurfaces. The metal stack has a thin Ti layer for adhesion to the GaAs substrate, and the Pt layer is a protection layer between the Au and Ti layers. Without the Pt layer, the metals diffuse into each other in the subsequent steps. If the Au and Ti diffuse together, the alignment mark becomes much less reflective, which makes precise alignment more difficult. The metasurface side is covered with a protective coating of 400 nm of SiN_x to protect the surface from the rest of the fabrication.

2. Sub-wavelength grating

The VCSEL side is patterned with the sub-wavelength grating for polarization pinning. The grating is etched into GaAs with sputtered 50 nm SiO_2 hard mask. Since the grating lines need to be sub-wavelength, the grating is patterned by EBL. Both the hard mask and the GaAs etch are performed with an inductively coupled plasma reactive ion etch (ICP-RIE), where the SiO_2 mask is etched with CF_4 and the grating in GaAs is etched down by a switched $SiCl_4$-O_2 etch. The switched process is also used to etch the optical dielectric metasurfaces, which is described in greater detail in the next chapter.

3. p-contact

The contact on the p-doped side of the DBR has the same metal stack of 20/50/100 nm Ti/Pt/Au as the alignment marks. The contact is only patterned on the VCSEL side of the chip for current injection. Since it is possible to highly p-dope GaAs with carbon, the top GaAs layer is doped to $5 \cdot 10^{19}$ cm^{-3}, and the metal stack forms a low resistive ohmic contact to the GaAs without any annealing. After the deposition, the ohmic connection is verified by the transfer length method (TLM).

4. VCSEL mesa etch

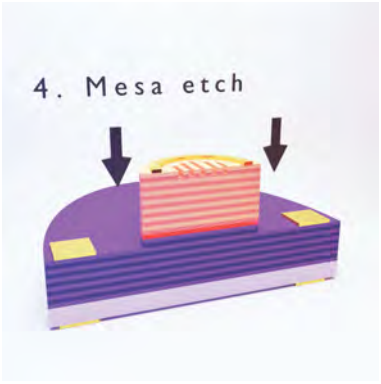

The mesa of the VCSEL needs to be etched down into the bottom n-doped DBR for deposition of the n-contact. Since the n-contact layer is 5 μm deep within the VCSEL epi, a sputtered 300 nm SiN_x hard mask for the GaAs etch is first patterned. The mesa is etched down by an AR-$SiCl_4$ ICP-RIE.

5. Selective wet oxidation

Most layers in the epitaxial stack are susceptible to oxidation since they contain Al. Therefore, a protective layer of SiN_x is first deposited and only etched open to expose the sidewalls of the VCSEL mesa. Since the entire bottom mirror and the top mirror are fully covered by SiN_x , any vertical oxidation is suppressed. The VCSEL chip is oxidized in a furnace at 410°C, where water vapor is introduced until the chamber reaches approximately 0.5 bar. The largest oxide aperture diameter for single-mode operation is $d_{ox} \approx$ 2-3 μm. On the chip, there are also several dedicated mesas at different positions that are patterned without the p-contact, called witness mesas. They can be etched down to the oxide aperture layer to directly image the achieved aperture diameter, giving an accurate estimation of the oxide apertures on the chip.

6. n-contact

The n-contact consists of an evaporated metal stack of 20/52/100 nm of Ni/Ge/Au. The n-type DBR is doped to $1 \cdot 10^{18}$ cm^{-3} with silicon. Since n-type doping with silicon cannot reach as high concentrations as p-type doping with carbon, the n-contact is annealed at 390°C to diffuse Ge into the GaAs substrate, which highly dopes the GaAs layer and creates a low resistive ohmic contact. Lastly, the ohmic contact is verified by TLM.

7. Passivation and bond pads

With all the contacts and the oxide aperture in place, the entire VCSEL surface is passivated with a sputtered 300 nm SiN_x film. As discussed with the polarization grating, the optical field has very low intensity at the top surface of the highly reflective top mirror, which implies that the lasing is largely unaffected by adding an additional layer on top of the VCSEL. The film is etched open for connection to the p- and n-contacts and 50/450 nm thick Ti/Au bond pads are sputtered for probing or wire bonding. Then, one more 300 nm thick SiN_x film is sputtered to protect the VCSELs from the subsequent metasurface fabrication. The last SiN_x layer is only etched open at positions for probing or wire bonding. Some of the bottom-emitting VCSELs are characterized without a metasurface, in the following section. A final SiN_x layer is sputtered on the metasurface side of these VCSELs to act as an anti-reflection coating, in order to reduce the reflections from the GaAs-to-air interface.

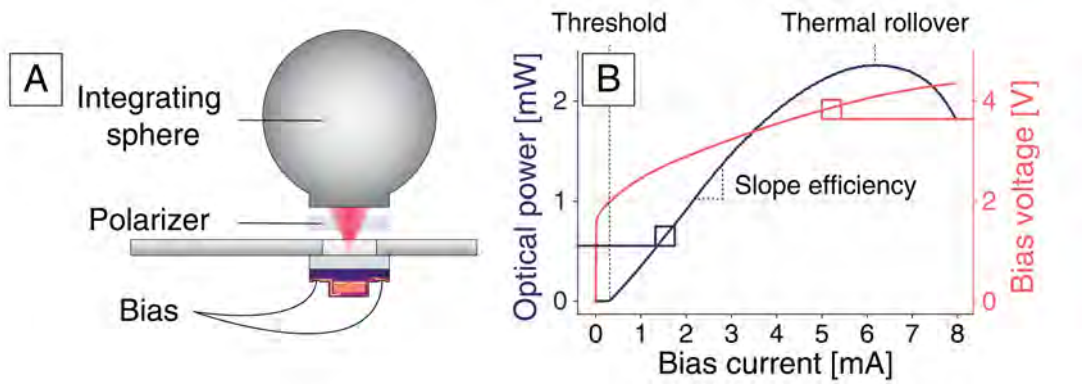

Figure 2.12: (**A**) The VCSEL chip is clamped to an aluminum holder with a hole so that an integrating sphere can be brought close enough to collect all light from the diode. (**B**) Current-Power-Voltage measurement of a single-mode GaAs VCSEL with an oxide aperture $d_{\mathrm{ox}} = 2\ \mu$m, without the polarizer.

2.2.4 VCSEL characterization

The VCSELs are characterized through three different types of characterizations: optical output power and voltage as a function of bias current, optical spectrum as a function of current, and far-field characteristics as a function of bias current.

Current-Optical output power-voltage measurement

The current-optical output power-voltage (IPV) relation is found by biasing the laser diode with a certain bias current, $\mathrm{I_b}$, while measuring the corresponding voltage, $\mathrm{V_b}$ and collecting all the light that is emitted, $\mathrm{P_{opt}}$, as shown in Fig. 2.12**A**. To collect all emitted light, an integrating sphere is brought close enough so the aperture collects all the light emitted from the VCSEL. Here, three characteristics of the VCSEL performance are considered: the threshold current $\mathrm{I_{th}}$, the slope efficiency $\frac{\mathrm{dP_{opt}}}{\mathrm{dI_b}}$, and maximum power at thermal rollover, $\mathrm{P_{max}}$. First, of the threshold current, $\mathrm{I_{th}}$, the current where the gain surpasses the loss in the cavity, $g > g_{\mathrm{th}}$, and the diode starts lasing. Secondly, the $\frac{\mathrm{dP_{opt}}}{\mathrm{dI_b}}$ is the linear increase in optical power with respect to increased bias current above the threshold. Finally, as $\mathrm{I_b}$ increases, the temperature in the cavity increases. This leads to both a mismatch between the gain spectrum with respect to the lasing wavelength, which reduces the gain experienced by the mode, i.e. modal gain. Moreover, the high thermal energy of the carriers causes them to be thermally excited over the MQW, which reduces the material gain. Both the reduction of modal

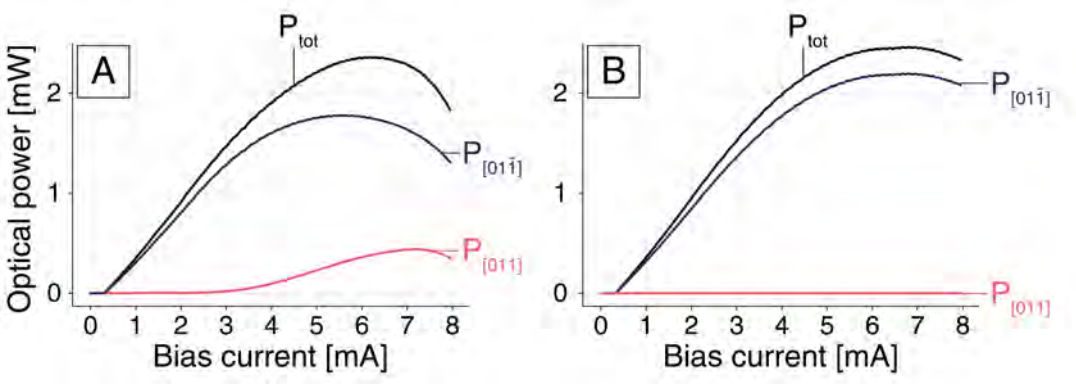

Figure 2.13: (**A**) Polarization resolved measurement for single-mode GaAs VCSEL with an oxide aperture $d_{ox} = 2\ \mu$m, without the sub-wavelength grating to pin the polarization. (**B**) The same measurement for a VCSEL with the sub-wavelength grating etched into the top mirror.

and material gain for larger bias currents causes P_{opt} to roll over and reduce when more current is supplied. The maximum optical output power is obtained at the thermal rollover. The final feature of the IPV curve for a bottom-emitting VCSEL is the ripple in P_{opt}; the ripple is due to the back reflection from the GaAs interface at the substrate. To minimize the effect, a $\lambda/4$ anti-reflection coating layer of SiN_x has been sputtered on all fabricated VCSELs without an optical metasurface, as mentioned before.

The polarization characteristics of the VCSEL are measured with the same IPV setup, but with a linear polarizer before the integrating sphere. As explained in the previous section, the fundamental mode can have two orthogonal polarization states with the electric field along the two principal axes of the GaAs crystal, the [011] and [01$\bar{1}$] directions for a GaAs substrate grown on a (100) oriented substrate. From small anisotropic differences in the crystal growth or induced by the fabrication, the two modes are slightly separated in wavelength. This separation causes the fabricated VCSELs to have a preferential lasing mode. The wavelength separation has the effect that the modes experience a different material gain or a different modal gain depending on how close they are to the peak of the gain spectrum. The state that experiences the highest gain will start to lase first, as can be seen in Fig. 2.13**A** the preferential state has a field oriented along the [01$\bar{1}$] axis. When the lasing starts, the high photon density consumes all available carriers and suppresses lasing of the other polarization state at low I_b. But, as mentioned, when I_b is in-

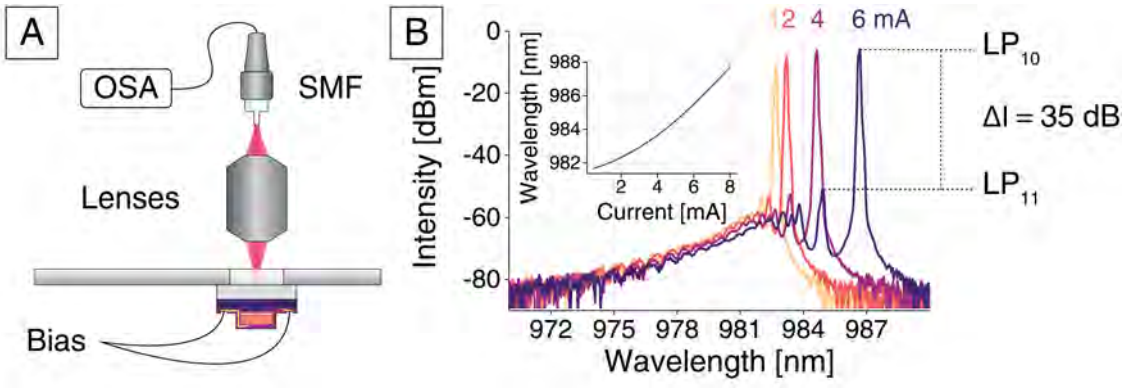

Figure 2.14: (**A**) The emitted beam is focused down on a tip of a SMF and fed to an OSA. (**B**) Spectral distribution of the quasi-single mode VCSEL with $d_{\mathrm{ox}} = 2\ \mu$m, for different bias currents, I_{b}. The intensity difference between the fundamental mode, LP_{01}, and the first higher order mode, LP_{11}, is beyond 30 dB which qualifies the VCSEL as quasi-single mode. In the inset the wavelength shift as a function of I_{b} is shown.

creased, both the gain spectrum and resonances start to shift, due to the increase in temperature. After a certain $\mathrm{I_b}$, the orthogonal polarization state [011] starts to lase, causing the polarization state of the emitted beam to drift. The polarization resolved measurements are performed by biasing the VCSEL slightly above threshold, and the linear polarizer is rotated to align with the preferential lasing state $[01\bar{1}]$ of the laser. After which the polarizer is rotated by $\pi/2$ to measure optical output power of the orthogonal state [011]. In Fig. 2.13**B** the same polarization resolved IPV is presented for the VCSEL with a sub-wavelength grating etched into the top-mirror, as discussed in Sec. 2.2.1, where it can be seen that the lasing in the orthogonal mode is suppressed.

Spectral measurement

To capture the spectrum of the laser, the emitted light is coupled into a fiber and fed to an optical spectrum analyzer (OSA), as in Fig. 2.14**A**. The measured spectral characteristics for several bias currents, $\mathrm{I_b}$, are presented in Fig. 2.14**B**, for a quasi single-mode VCSEL. In the spectrum, the broadband emission from the gain spectrum from the MQW can be seen as the emitted light that has an intensity above the noise floor. In the gain spectrum, there are several peaks that come from the different higher-order transverse modes; the fundamental mode, LP_{01}, has the longest wavelength as discussed before in Sec. 2.2.1. The SMSR is calculated as the difference in intensity between the fundamental mode

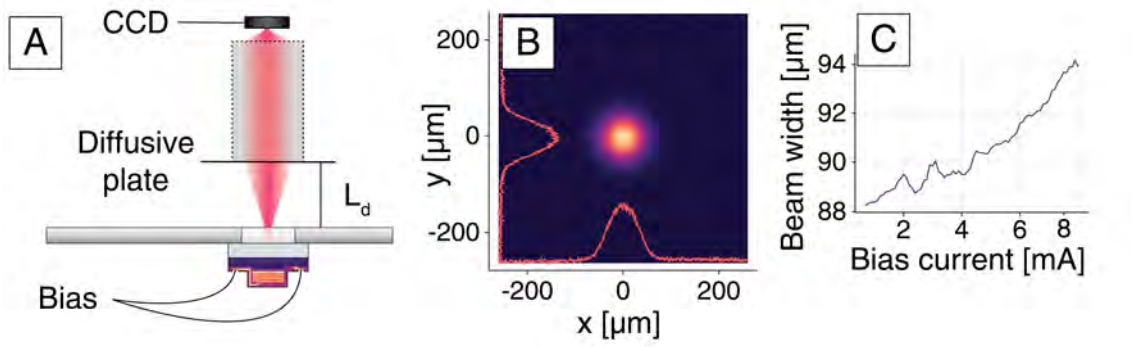

Figure 2.15: (**A**) Measurement setup for the beam width of a VCSEL. (**B**) Analytically propagated field by L_d to the substrate of the VCSEL. (**C**) The beam width dependency of the bias current, which increases mainly due to thermal lensing from the increase in temperature.

and the higher-order mode with the highest intensity, and as mentioned, a VCSEL is termed quasi single-mode with SMSR $>$ 30 dB. Finally, the measurement in Fig. 2.14**B** is performed for the same VCSEL as in Fig. 2.12, where the second polarization has significant power for $\mathrm{I_b} > 3$ mA; however, the spectrum measurement only shows one lasing peak for the fundamental, leading to the conclusion that the two lasing polarizations are separated in wavelength smaller than the resolution of the OSA, $\Delta\lambda < 0.2$ nm. Lastly, as an inset in Fig. 2.14**B** an inset of the wavelength shift with respect to I_B, which increases due to the increase in the refractive index of the cavity due to the increase in temperature.

Far-field emission

The final characterization is performed to find the beam width, $1/e^2$, of the beam when it is leaving the GaAs substrate, the width that the beam will have when it is illuminating the optical metasurface. The VCSEL is again biased, and the emitted beam illuminates a diffusive plate at a distance L_d from the substrate. The resulting image on the diffusive plate is imaged by a lens onto a charge-coupled device (CCD) camera, as presented in Fig. 2.15**A**. From the imaged beam, the divergence of the beam can be calculated, which allows us to analytically back propagate the beam by L_d back to the substrate. The analytically propagated beam that will be incident on the metasurface is presented in Fig. 2.15**B** for the bias current $I_\mathrm{b} = 1$ mA. Finally, the beam width of the emitted beam changes with the bias current due to the temperature increase of the cavity. The effect is known as thermal lensing, where the temperature

increase leads to a refractive index profile that provides an additional focusing effect of the beam from the cavity. The additional lensing effect leads to a greater divergence of the emitted beam, which leads to an increase of the beam width with bias current, I_{b}. In Fig. 2.15**C** the $1/e^2$ beam width of the beam that is incident on the substrate of the bottom-emitting VCSEL is presented as a function of the bias current, I_{b}.

CHAPTER 3

Monolithically integrated metasurfaces

The metasurface is a two-dimensional metamaterial, artificially structured materials with sub-wavelength constituents, that exhibit extraordinary behavior when illuminated, allowing for the construction of, for example, perfect lenses [82] or electromagnetic invisibility cloaks [83]. Metamaterials utilize a spatial modification of the dielectric function, ϵ and μ, by sub-wavelength nanostructures, called metaatoms. However, the above examples utilize the plasmonic response of metallic metaatoms that are stacked in three dimensions. Since metals are associated with a large attenuation, and because it is an enormous nanofabrication task to construct three-dimensional sub-wavelength structures, for optical wavelengths, the beam-shaping of light is mainly performed with dielectric metasurfaces [84].

Contrary to the three-dimensional metamaterials, a two-dimensional metasurface relies on structuring metaatoms on a surface, which can introduce abrupt changes to amplitude, phase, and polarization. The dielectric metasurface has been shown to be able to extensively control light, being able to replicate essentially any function of a classic refractive optical element and outperform them in some cases. In addition, it is possible to combine several functionalities into one single surface, with a thickness of the same order as the wavelength.

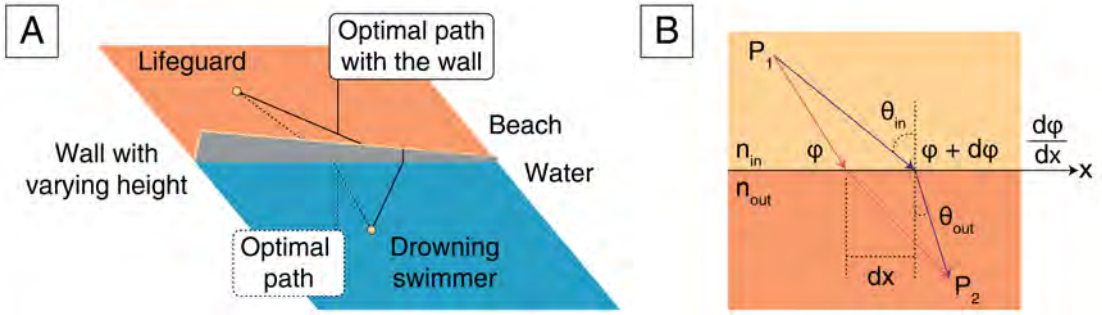

Figure 3.1: (**A**) Analogy for the generalized Snell's law, a lifeguard is in a hurry to save a drowning swimmer. The height of wall on the border between the beach and water will determine the optimal path for the lifeguard. The phase gradient from the metasurfaces functions as a wall with a varying height, but for light. (**B**) The schematics for the derivation of generalized Snell's law. If the interface between n_{in} and n_{out} has a spatially dependent phase, $\frac{\mathrm{d}\phi}{\mathrm{d}x}$, the direction of the refracted beam can be arbitrarily controlled.

3.1 Shaping light with sub-wavelength nanostructures

Classical refractive elements, such as a lens, shape the phase profile of a transmitted beam by a laterally varying phase accumulation from the curved surface of the lens. Metasurfaces are sub-wavelength structured surfaces that impart a designed phase profile and amplitude on the transmitted wave. Snell's law can be generalized by introducing a phase gradient along the interface between two different media as [37]

$$n_{\text{in}} \sin\theta_{\text{in}} - n_{\text{out}} \sin\theta_{\text{out}} = \frac{\lambda_0}{2\pi} \frac{\mathrm{d}\phi}{\mathrm{d}x}. \tag{3.1}$$

Here $\frac{\mathrm{d}\phi}{\mathrm{d}x}$ is the phase gradient along the interface, n_{in} and n_{out} are the refractive indices of the incident and outgoing media, θ_{in} and θ_{out} are the respective resulting angles. In Fig. 3.1**A** an analogy for the generalized Snell's law is presented, by extending the high school analogy for Fermat's principle, where a lifeguard wants to save a drowning swimmer. Fermat's principle says that light will take the fastest route between two points, which is equivalent to saying that light takes the path with the smallest amount of accumulated phase. In the analogy, a lifeguard wants to save a drowning swimmer. The lifeguard is in a hurry and wants to take an optimal path, knowing that it is faster to run on the beach than to swim in the water. To arrive at generalized Snell's law, the lifeguard

also has to consider the time it takes to climb a wall with varying height on the border from the beach to the water. By controlling the height variation of the wall, it is possible to control the optimal paths from any starting position for the lifeguard to any position of a drowning swimmer. The phase gradient in the generalized Snell's law functions just as a wall with a varying height, where the amount of accumulated phase is dependent on where light is incident on the interface. Eq. 3.1 is found by applying Fermat's principle and simple trigonometry for an interface that imparts a varying amount of accumulated phase, an interface with a gradient of accumulated phase, $\frac{\mathrm{d}\phi}{\mathrm{d}x}$, as shown in Fig. 3.1**B** [37]. Just as for the optimal path for the lifeguard, generalized Snell's law implies that the direction of the refracted beam can be arbitrarily controlled by the introduction of the phase gradient. As with refractive optical elements, the phase profile of the metasurface needs to be able to span 0-2π to achieve arbitrary beam shaping, which is known as full phase coverage.

By replicating the spatially varying phase profile of any classical refractive optical element, the needed phase gradient, Eq. 3.1, to achieve a desired beam can be computed. For example [65], the phase profile of a lens for focusing or collimation of a beam, an axicon to produce Bessel beams, or a blazed grating for deflection,

$$\begin{aligned}
\phi_{\text{lens}} &= -\frac{2\pi n_{\text{out}}}{\lambda}\sqrt{x^2+y^2-f^2}-f,\\
\phi_{\text{axicon}} &= -\frac{2\pi n_{\text{out}}}{\lambda}\text{NA}\sqrt{x^2+y^2},\\
\phi_{\text{blazed}} &= -\frac{2\pi n_{\text{out}}}{\lambda}\left[x\sin\Theta_x + y\sin\Theta_y\right],
\end{aligned} \tag{3.2}$$

where f is the focal length of the lens, NA$=\sin\alpha$ is the numerical aperture in air for the axicon, and Θ_x, Θ_y are the deflection angles for the grating. Beyond phase profiles that replicate known optical elements, it is possible to start from an arbitrary electric field that is desired some distance away from the metasurface. Then numerically backpropagates the field to the metasurface plane and finds the phase distribution that generated the field. This methodology is popular for the projection of holograms [85] with metasurfaces or diffractive optical elements, and typically the Gerchberg–Saxton algorithm is used to quickly compute the needed phase distribution [86].

A metasurface will not only impart a laterally dependent phase on an in-

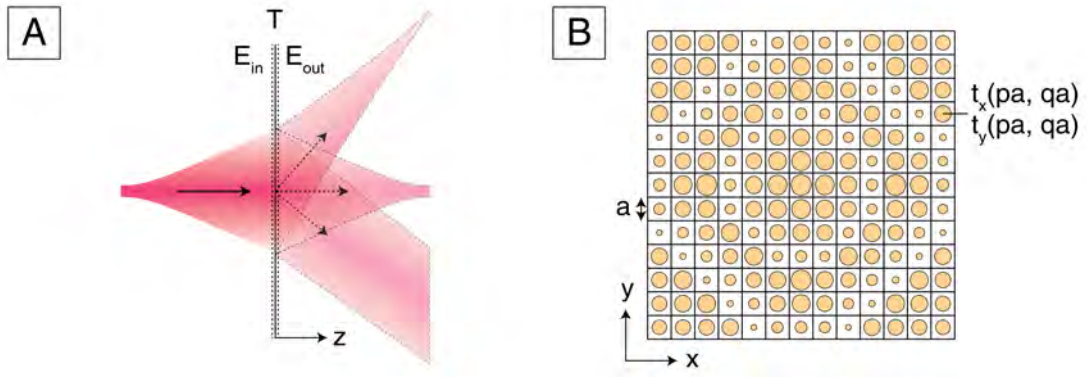

Figure 3.2: (**A**) Three alternatives for beam shaping of a divergent beam, $\mathbf{E}_{\text{in}}$, from a metasurface with the transfer function $\mathbf{T}$. (**B**) Discretized rectangular lattice for a phase gradient metasurface. Every metaatom has an individual complex transfer coefficient, t_x and t_y.

cident beam, but also a laterally dependent amplitude. The modulation due to a metasurface can generally be written as a spatially dependent complex transfer function,

$$\mathbf{E}_{\text{out}}(x,y) = \mathbf{T}(x,y)\mathbf{E}_{\text{in}}(x,y) = \begin{bmatrix} t_x(x,y) & 0 \\ 0 & t_y(x,y) \end{bmatrix} \begin{bmatrix} E_x(x,y) \\ E_y(x,y) \end{bmatrix}, \quad (3.3)$$

where $\mathbf{E}_{\text{out}}$ and $\mathbf{E}_{\text{in}}$ are the outgoing and incident beams on the metasurface, and $t = |t|e^{j\phi}$ are complex transmission coefficients for the incident beam, for respective polarization, at position x and y in the metasurface, as shown in Fig. 3.2**A**. Noteworthy is that an arbitrary beam can be produced by the imparted phase, Eq. 3.1. Since adding the phase from a second transfer function corresponds to a linear operation, it is possible to stack several beam shaping phase gradients into one single transfer function and realize it with a single metasurface. Finally, the reflection from the metasurface can be written in the same way.

3.1.1 Phase gradient metasurfaces

The conventional way to design phase gradient metasurfaces is called phase-mapping, where $\mathbf{T}$ is approximated by discretizing it in a sub-wavelength periodic lattice as

$$\mathbf{T}(x,y) \approx \sum_{p,q} \hat{\mathbf{T}}(pa,qa) = \sum_{p,q} \begin{bmatrix} \hat{t}_x(pa,qa) & 0 \\ 0 & \hat{t}_y(pa,qa) \end{bmatrix}, \quad (3.4)$$

where $\hat{\mathbf{T}}(pa,qa)$ is the transfer function for one metaatom at position (pa,qa), a is the lattice constant of the rectangular grid, and p and

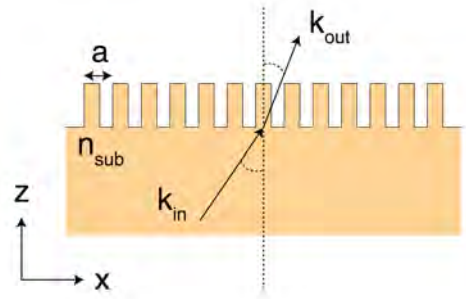

Figure 3.3: When the lattice constant is smaller than the wavelength in the substrate of a metasurface, $a < \lambda/n_{\text{sub}}$, all higher orders of diffraction are suppressed.

q are integers. The discretization is exemplified in Fig. 3.2**B**. Each metaatom samples the phase profile at a discrete point in the lattice of the metasurface. Since the phase-mapped metasurface is discretized in a periodic lattice, the metasurface can add momentum and diffract the incident beam. By limiting the lattice constant, in a rectangular lattice, to be smaller than the wavelength in the substrate, any higher order of diffraction can be suppressed. The condition for suppressing higher diffraction orders is found by considering added momentum from the lattice and the dispersion relation in free space,

$$k^2 = k_z^2 + k_x^2, \quad k_{x,\text{in}} + \frac{2\pi}{a}m = k_{x,\text{out}} \quad \rightarrow \quad a < \frac{\lambda_0}{n_{\text{sub}}}, \tag{3.5}$$

where $k_{x,\text{in}}$ and $k_{x,\text{out}}$ are the in-plane momentum of the beam incident on the metasurface, and m is an integer. If the lattice constant a fulfills the above condition, all higher diffraction orders will have a purely imaginary propagation constant in the direction of propagation, which means that the field is evanescent and does not propagate any energy. The metasurface and the corresponding momentum are shown in Fig. 3.3.

Equipped with a discretized transfer function, $\hat{\mathbf{T}}(pa, qa)$, the individual metaatoms that can be fabricated and have full phase coverage need to be designed. In the phase mapping approach, Maxwell's equations are solved for a range of different metaatoms to create a mapping between the geometry of the metaatom to the respective complex transfer coefficients, $\hat{t}_x$ and $\hat{t}_y$. With the mapping, the final step is to construct the

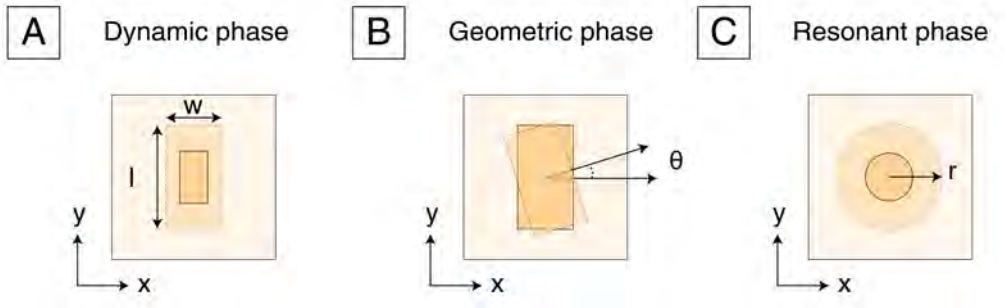

Figure 3.4: The three main metaatoms for phase gradient metasurfaces. For dynamic phase the size of the metaatom, w and l, is varied to change the effective refractive index, n_{eff}. In geometric phase one metaatom is rotated to produce the desired phase gradient. Finally, in the resonant phase a metaatom with Mie-resonance is changed in size.

metasurface by placing metaatoms in the specified grid to approximate $\mathbf{T}(x, y)$. Generally, the design of phase gradient dielectric optical metasurfaces is divided into three main categories: dynamic, geometric and resonant phase.

Dynamic phase metasurfaces

For a dynamic phase metasurface, also referred to as propagation phase or effective waveguide index metasurfaces, the dimensions of the metaatom are changed to create the different phase delays, as seen in Fig. 3.4A. Since the material of the substrate has a larger refractive index than the surrounding medium, changing the size of the etched metaatoms leads to a change in the effective refractive index of each unit cell,

$$\hat{t}_{\text{dynamic}} = |\hat{t}|e^{j\frac{2\pi}{\lambda}hn_{\text{eff}}}, \tag{3.6}$$

where λ is the free-space wavelength, h is the height of the metasurface, and n_{eff} is the effective index of the unit cell. From the existence of geometric Fabry-Pérot resonances, the effective index in Eq. 3.6 is not a linear function of the area of the metaatom; thus, electrodynamic simulations are needed to accurately design the phase delay. Secondly, the simulations are necessary to find the transmission amplitude, $|\hat{t}|$, of the metaatoms. Finally, an anisotropic metaatom can impart a different phase delay for each of the principal axes, and thus alter the polarization state of the incident beam. For example, the metaatom in Fig. 3.4A will have a different effective index for the x-axis, compared to the y-axis.

Geometric phase metasurfaces

The geometric phase metasurface, or Pancharatnam-Berry metasurface, got its name from the discovery and generalization of geometric phase by Pancharatnam [87] and Berry [88]. The geometric phase metasurface is created by an anisotropic metaatom, referred to as a nanofin, that creates a different refractive index for an incident beam along two different principal axes of the unit cell, as shown in Fig. 3.4B. The nanofin can then be rotated to create the phase gradient. The principle is straightforward to show with Jones calculus, where the transfer function from one nanofin, at a certain position in the metasurface lattice, (pa, qa), can be rotated by the angle θ as

$$\begin{aligned}\hat{\mathbf{T}}_{\mathrm{pb}}(\theta) &= \mathbf{R}(-\theta)\begin{bmatrix}\hat{t}_x & 0\\ 0 & \hat{t}_y\end{bmatrix}\mathbf{R}(\theta)\\ \hat{\mathbf{T}}_{\mathrm{pb}}(\theta) &= \begin{bmatrix}\hat{t}_x\cos^2\theta + \hat{t}_y\sin^2\theta & \left(\hat{t}_x - \hat{t}_y\right)\sin\theta\cos\theta\\ \left(\hat{t}_x - \hat{t}_y\right)\sin\theta\cos\theta & \hat{t}_x\sin^2\theta + \hat{t}_y\cos^2\theta\end{bmatrix},\end{aligned} \tag{3.7}$$

where $\hat{t}_x$ and $\hat{t}_y$ are the complex transmission coefficients for the polarization along the two principal axes of the nanofin. For an incident linearly polarized beam, $\mathbf{E}_{\mathrm{linear}} = \begin{bmatrix}1\\0\end{bmatrix}$, the resulting beam field becomes

$$\hat{\mathbf{T}}_{\mathrm{pb}}(\theta)\mathbf{E}_{\mathrm{linear}} = \left[\frac{\hat{t}_x + \hat{t}_y}{2} + \frac{\hat{t}_x - \hat{t}_y}{2}e^{2i\theta}\right]\vec{r} + \left[\frac{\hat{t}_x + \hat{t}_y}{2} + \frac{\hat{t}_x - \hat{t}_y}{2}e^{-2i\theta}\right]\vec{l}, \tag{3.8}$$

where $\vec{r}$ and $\vec{l}$ are the basis vectors for right-handed and left-handed circularly polarized light, respectively. The phase of the second term, with $e^{\pm 2i\theta}$, for each handedness, is determined by the rotation of the nanofin, and the phase shift due to this rotation, $\pm 2\theta$, is known as the geometric phase. The first term can be canceled by designing the transmission coefficients, t_x and t_y, to produce a relative π-shift, meaning that each nanofin functions as a half-wave plate. Without the first terms Eq. 3.8 reduces to

$$\hat{\mathbf{T}}_{\mathrm{pb}}(\theta)\mathbf{E}_{\mathrm{linear}} = \frac{1}{\sqrt{2}}e^{2i\theta}\vec{r} + \frac{1}{\sqrt{2}}e^{-2i\theta}\vec{l}, \tag{3.9}$$

which implies that the geometric phase will be imparted with a different sign into each handedness of the linear polarized beam. If the phase gradient is designed to focus light, an incident linearly polarized beam will be split into a focused right-handed polarized beam and one diverging left-handed polarized beam. This implies that if the geometric phase

metasurface is illuminated by a VCSEL, lasing with a linearly polarized beam, it is only possible to design the geometric phase for half of the intensity. The other half will get modulated with the same phase gradient, but with the opposite sign.

Resonant phase

The early stage of phase gradient metasurfaces was created by phase shifts from plasmonic resonances. However, due to the large attenuation corresponding to using metals at optical frequencies, the technique was generalized to using dielectric metaatoms that support different orders of electric and magnetic Mie resonances [84]. The transmittance and the reflectance of electric and magnetic Mie-type resonances, approximated as Lorentzian resonances, are found as

$$\begin{aligned} \hat{t}_{\text{resonant}} &= 1 + \frac{2i\gamma_e\omega}{\omega_e^2 - \omega^2 - 2i\gamma_e\omega} + \frac{2i\gamma_m\omega}{\omega_m^2 - \omega^2 - 2i\gamma_m\omega}, \\ \hat{r}_{\text{resonant}} &= \frac{2i\gamma_e\omega}{\omega_e^2 - \omega^2 - 2i\gamma_e\omega} - \frac{2i\gamma_m\omega}{\omega_m^2 - \omega^2 - 2i\gamma_m\omega}, \end{aligned} \tag{3.10}$$

where γ_e and γ_m, are the damping coefficients for the electric and magnetic induced dipoles respectively, ω_e and ω_m, are the angular frequencies of the electric and magnetic resonances. By tuning the dimensions of the Mie particle, it is possible to have the resonances overlap, $\omega_e = \omega_m$ with damping coefficients; this creates a perfect destructive interference of the reflection and gives unity transmission, known as the Kerker condition. However, since the functionality comes from being close to the resonances of the metaatoms, the method sets a very high requirement on the fabrication tolerances.

3.2 Diffractive unit cell metasurfaces

In the conventional phase mapping approach to design metasurfaces, the lattice constant is, as mentioned, usually set to be sub-wavelength to suppress all higher orders of diffraction, Eq. 3.5. One limitation for the phase mapping approach is that the individual metaatom samples the phase gradient at discrete points in the lattice. Thus, the sampling rate is limited by the periodicity of the lattice, which in turn is limited by how small lattice constant, a, that can be fabricated. Therefore, the

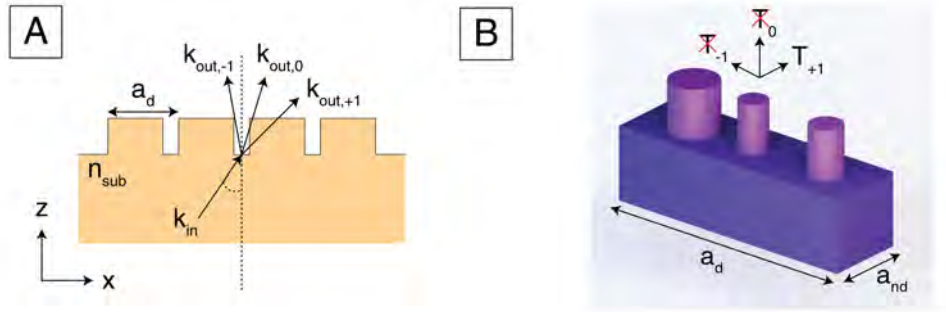

Figure 3.5: (**A**) Added momentum from a metasurface with a large periodicity allows for higher diffraction order. (**B**) The supercell for diffractive metasurface. By changing the size and position of the metaatoms inside the supercell, constructive interference can take place in all but one wanted diffraction order.

phase mapping approach cannot resolve arbitrarily steep phase gradients, which are required to efficiently deflect light to large angles. As seen in Eq. 3.2 for the blazed grating, the deflection angle, Θ_x or Θ_y, are scaling constants for how rapidly the phase profile should change laterally.

One solution to the limited phase sampling is called the diffractive metasurfaces [43]. In contrast to the phase mapping approach, the unit cell has larger periodicity, referred to as a diffractive lattice constant a_d, than the wavelength in the substrate, intentionally opening up higher orders of diffraction. By, again, considering the added momentum from the metasurface and the dispersion relation in free space,

$$k^2 = k_z^2 + k_x^2, \quad k_{x,\mathrm{in}} + \frac{2\pi}{a_\mathrm{d}} m = k_{x,\mathrm{out}} \quad \rightarrow \quad a_\mathrm{d} > \frac{\lambda_0}{n_\mathrm{sub}} m, \tag{3.11}$$

where, as long as the inequality is fulfilled, the mth diffraction order corresponds to a propagating solution. The diffractive metasurfaces and the corresponding momentum can be seen in Fig. 3.5**A**. In the other dimension, the lattice constant is, again, smaller than the wavelength in the substrate to suppress all higher orders of diffraction, and labeled as the non-diffractive lattice constant, a_nd. However, with a large periodicity, several metaatoms can be placed in each unit cell; these larger unit cells with several particles are referred to as a supercell. Each metaatom in the supercell will impart its own amplitude and phase contribution for each of the diffraction orders. Thus, the geometry and position of the

particles inside the supercell can be designed to create destructive interference in all but one desired diffraction order, as shown in Fig. 3.5**B**, with the deflection angle set by the grating equation

$$\sin\left(\theta_{\mathrm{out,m}}\right) = \frac{\lambda}{a_{\mathrm{d}} n_{\mathrm{s}}} m. \tag{3.12}$$

The diffractive metasurface circumvents the limitation of the sampling rate in the phase mapping approach by setting the deflection angle with the diffractive periodicity, a_{d}, of the supercell. The one-dimensional version of the diffractive metasurface, where the metaatoms of the supercell are grating lines, is referred to as a metagrating. A noteworthy result for the metagrating is that it has been theoretically shown that it is always possible to find a configuration that has a unity relative transmission into the desired diffraction order [89].

3.3 GaAs dielectric metasurface fabrication

The intention is to monolithically integrate the designed metasurfaces into the GaAs substrate of the bottom-emitting VCSELs described in the previous chapter. GaAs is a dielectric material with a high refractive index, $n_{\mathrm{GaAs}} = 3.52$ at 980 nm. The high refractive index increases the modulation from the geometry of the metaatom, since a higher refractive index amplifies the electric field within the metaatom. Generally, this relaxes the nanofabrication, since it is possible to achieve 2π phase coverage by metaatoms of smaller height. For example, the dynamic phase delay, Eq. 3.6, is proportional to the effective refractive index, n_{eff}, and the height of the metaatom, h. By increasing n_{eff} the height can be reduced. The processing of the metasurface is performed after the laser diode is complete, since the fabrication of the laser diode involves deep etching of GaAs, which could potentially damage the metasurface. Since the metasurface is a delicate nanostructure that will modulate the phase of light, it is of the highest importance that the backside of the chip is as pristine as possible during the laser diode fabrication to etch a functional and efficient metasurface in the substrate.

3.3.1 Aspect-ratio dependent etching

An inherent problem with monolithic integration is the lack of an etch stop layer. When etching without an etch stop, larger gaps in an ex-

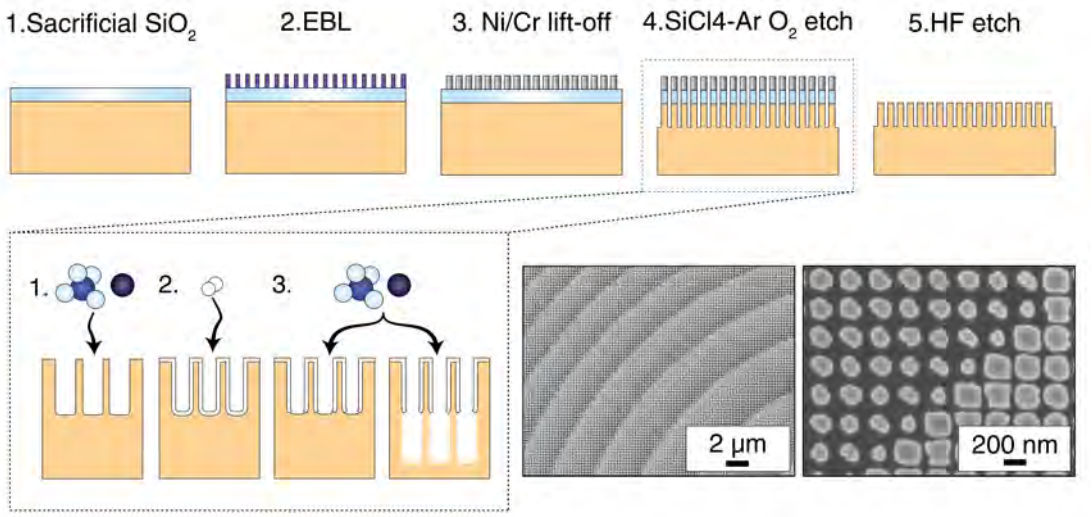

Figure 3.6: Fabrication of GaAs metasurfaces. The positive resist ARP6200 is exposed to create metal mask for the GaAs-etching. The inset shows the steps for the switched $SiCl_4$-Ar etching. The switched etching mimics bosch etching, where the $SiCl_4$-Ar etching steps are cycled by flushing O_2 for sidewall passivization. The final two SEM images are of fabricated metasurfaces, designed by a conditional generative adversarial network [90], that replicates the phase profile of a lens, Eq. 3.2, with focal length 600 μm.

posed pattern are usually etched deeper than smaller gaps, due to the easier access of etching reagents, which is known as aspect-ratio dependent etching (ARDE). To design an efficient monolithically integrated metasurface, the ARDE needs to be taken into account. One solution is to find the etch rate dependency for different gaps and take that into account in the design process. The other approach is to design a metasurface that only uses the same gaps in the exposed pattern, since that automatically leads to all gaps being etched to the same depth. In this work, mainly the second approach has been considered, which is further discussed in the next chapter.

3.3.2 Metasurface process flow

The advantage of the metasurface over its predecessor, diffractive optics, is that only one etching step is needed to fabricate the entire metasurface. The monolithically integrated GaAs metasurfaces are etched by an ICP-RIE process with a metal mask. The high selectivity of a metal mask is needed, since the height of the metaatoms generally needs to be on

the order of one wavelength to achieve full 2π phase coverage. The full process step is presented in Fig. 3.6 and described here.

1. Sacrificial SiO_2

First step is to sputter a sacrificial layer for the metal hard mask. SiO_2 is chosen since it is easy to remove after the metasurface etch by a buffered oxide etch (BOE) or hydrofluoric (HF) acid wet etch. The sacrificial layer should be as thin as possible to minimize distortion of the etched pattern; however, with a too thin layer, the metal can stick to the metasurface after the sacrificial layer wet etch. Since metal is associated with a high absorption and will distort the designed modulation of the dielectric metaatoms, which is highly undesirable. For the metasurface fabrication the sputtered SiO_2 is set to 25 nm, which allows for a clean removal of the metal hard mask.

2. Electron beam lithography

Since the metaatoms are sub-wavelength, EBL is needed to pattern the mask for the optical dielectric metasurface. The surface is prepared by dehydration baking, at 160°C to remove surface moisture and volatile surface compounds, and covered with hexamethyldisilazane (HMDS), that reacts with any leftover surface moisture and forms a hydrophobic layer, which increases the resist adhesion. The resist for the fabrication is ARP6200 diluted by a 1:1 ratio with thinner, which results in a 120 nm resist film for the EBL. The ARP-resist is developed by n-amyl acetate and rinsed with isopropyl alcohol (IPA). Since it is an organic developer with a hydrocarbon chain that is non-polar, n-amyl acetate is hydrophobic and cannot be properly rinsed by only deionized water.

3. Metal hard mask lift-off

The metal stack for the hard mask is evaporated 10/50 nm Ni/Cr, where the Ni serves as the adhesion layer to the substrate surface and the Cr as the etch mask. To have minimal distortion of the designed pattern, the metal stack should be as thin as possible. However, the metal film also needs to be cleanly removed after the etch. With a too thin metal film, the mask has a tendency to break up into small shards of metal that spread everywhere in the solvent for the lift-off, making it impossible to ensure that all metal is properly removed. With the 10/50 nm Ni/Cr metal stack, the film lifts off as one continuous piece where the pattern

is connected, ensuring that all metal is removed. The lift-off for this fabrication is performed in an organic solvent-based remover MR-rem 400. The metal stack has a high selectivity to the subsequent etch; patterns as deep as 1.4 μm have been etched into GaAs without any notable degradation to the metal mask.

4. Metasurface etch

First, the sacrificial SiO_2 layer is etched with an ICP-RIE by a CF_4 plasma. The metasurface etch is performed with a switched etching process that mimics the Bosch process for silicon, as seen in the inset of Fig. 3.6. The switch process cycles between etching with a $SiCl_4$ and Ar plasma and sidewall passivization by injecting O_2 to form SiO_2 passivation of the sidewalls. The switched process cycles between three steps. In the first step, GaAs is etched using $SiCl_4$ and Ar plasma. The $SiCl_4$ gas separates into Si and Cl_2, and Cl_2 chemically etches the GaAs, while the Ar ions physically etch the GaAs. In the second step, the sidewall passivation of SiO_2 is formed by an O_2 plasma, where the oxygen reacts with the remaining Si from the GaAs etching step. These two steps are cycled between until the design depth is reached. The deeper the etching is performed, a slight tilt inwards of the metaatom occurs. This comes from the decreasing access of etching reagents. To counteract the tilt, the time of the etching step is increased the longer the etch is performed.

5. Sacrificial SiO_2 wet etch

To finally remove the metal mask, the sacrificial SiO_2 film is removed by a BOE or HF wet etch. The chip is stirred during the wet etch to minimize the metal that electrostatically attaches to the GaAs substrate. Lastly, the chip is rinsed with water and properly cleaned before characterization.

3.4 Fourier plane imaging for metasurface characterization

The main characterization for both the stand-alone GaAs metasurfaces and the VCSEL with facet-etched metasurfaces' performance is done with Fourier plane imaging. An inverted microscope is set up as shown in Fig. 3.7**A**. The objective is focused on the plane of the metasurface;

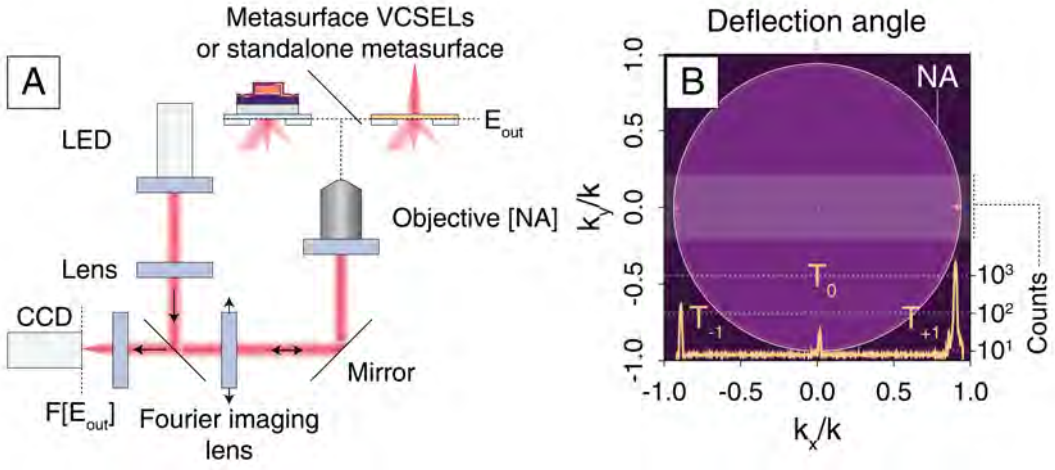

Figure 3.7: (**A**) Inverted microscope setup for Fourier plane imaging to characterize stand-alone metasurfaces or VCSEL with facet-etch metasurfaces. The light emitting diode (LED) is used to illuminate metasurface plane to be able to focus the imaging. (**B**) Fourier plane image of a diffractive metasurface that is illuminated by a plane wave. The first diffraction orders are open, but interference from the metaatoms channel almost all light into the +1 diffraction order at 65° or $k/k_x = 0.906$. The lower inset is an integrated cross-section of the image in logarithmic scale.

in the back-focal plane of the objective, the spatial frequencies or momentum of $\mathbf{E}_{\text{out}}$ are separated laterally. By placing a lens that in turn images the back-focal plane onto the CCD camera, the measured image corresponds to the spatial frequency or momentum of $\mathbf{E}_{\text{out}}$. The spatial frequencies of a theoretically desired beam can easily be computed by the Fourier Transform of desired $\mathbf{E}_{\text{out}}$ and can be compared to the measured image. An example of a standalone diffractive metasurface illuminated by a plane wave is presented in Fig. 3.7**B**, where the metasurface is designed to deflect light to a large angle of 65°. The highest possible momentum of light that can be imaged is limited by the numerical aperture of the objective

$$\text{NA} = n_{\text{obj}} \sin \theta_{\text{obj}}, \tag{3.13}$$

where n_{obj} is the refractive index of the medium where the objective is collecting light and θ_{obj} is the largest angle that can be collected. Finally, the relative transmission efficiency is characterized by measuring the ratio of the intensity of the desired beam to the total transmitted intensity. Exemplified with the relative transmission efficiency of the diffractive metasurface, in Fig. 3.7**B**, where the relative transmission

efficiency is calculated as

$$\eta_{\mathrm{rel}} = \frac{I_{+1}}{I_{-1} + I_0 + I_{+1}}, \tag{3.14}$$

where I_{-1}, I_0 and I_{+1} are the intensities of the three different diffraction orders.

CHAPTER 4

Integrated biophotonics

Biophotonics is an interdisciplinary field that combines biology and photonics to explore and manipulate biological systems using light. Advanced tools, such as fluorescence microscopy [91], super-resolution microscopy [92], optical coherence tomography [93], or optical tweezers [94], provide insight by peering into the otherwise unseen. Biophotonics is pivotal in medical diagnostics, disease treatment, and research by enabling the monitoring of molecular or cellular processes. Driven by an ever-growing demand and curiosity to image or sense new things, an enormous range of biophotonics techniques and devices have emerged in the literature in recent decades [95].

4.1 Miniaturized integrated biophotonics

The small footprint of the VCSEL with a facet-etched metasurface holds potential for the miniaturization of several of the above-mentioned examples of biophotonics devices. All the mentioned techniques start by having the proper illumination source to enable the sensing. Since the metasurface integrated VCSEL directly produces an arbitrary beam from the chip, it can remove the need for any external optics. This miniaturization step can pave the way for advanced biophotonics to reach new areas, such as in point-of-care applications, where it is impossible to set up a bulky optical setup. Further, every VCSEL can have its own meta-

surface; it is possible to produce a chip that can produce a plethora of beams for different purposes. These VCSEL chips are a suitable candidate for the illumination source for lab-on-a-chip devices, where the chip integrated together with microfluidics could perform several different sensing techniques simultaneously. For this work, two such illumination modules for biophotonics have been miniaturized, enabled by the VCSEL with a facet-etched metasurface. The first is an illumination module that can rapidly switch between two different modes in high-contrast microscopy, dark-field (DF) and total internal reflection (TIR), and the second module is a miniaturized illumination source for angle-resolved surface plasmon resonance (SPR) sensing.

4.2 Metagratings for high angle deflection and quasi-collimation

For both of the presented modules, the desired beam is a line of light at a steep angle, referred to as a fan-shaped beam. Most of the light should be deflected to a larger angle than the critical angle of a glass-air interface. The critical angle is found from Snell' law as,

$$\theta_{\mathrm{c}} = \arcsin\left(\frac{n_{\mathrm{out}}}{n_{\mathrm{in}}}\right), \tag{4.1}$$

where light at a larger angle than θ_{c} will be reflected back from the surface. However, the total internally reflected light still produces an evanescent field that extends beyond the interface, with a penetration depth of the same order as the wavelength. The short extent of the evanescent field can be utilized to construct a sensor or imaging device that only senses or creates images of molecules or particles that are in very close proximity to the interface. To have total internal reflection illumination in a suitable environment for biophotonics, light needs to be deflected to a large angle. For example, if the illumination source is incident from a glass medium, $n_{\mathrm{in}} = 1.51$, and illuminating a sample dispersed in water, $n_{\mathrm{in}} = 1.33$, the critical angle is $\theta_{\mathrm{c}} = 62.0°$. Preferably, all light from the illumination source should be above the critical angle.

For deflection of light, the diffractive metasurface, as discussed in Sec. 3.2, has the advantage of being able to produce very steep angles with maintained efficiency. Furthermore, it is also possible to circumvent the ARDE, mentioned in Sec. 3.2, associated with monolithic integration,

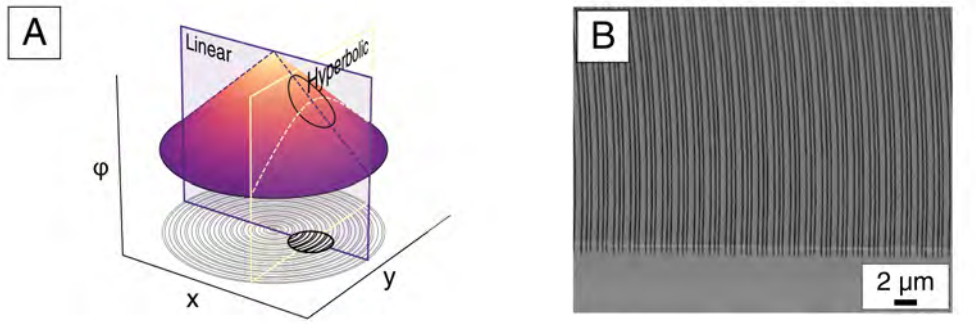

Figure 4.1: (**A**) Phase profile for the offset-axicon metagrating. By an offset x_0 along the x-axis the phase profile becomes linear along the x-axis and hyperbolic along the y-axis. (**B**) SEM image with a tilted view of a cleaved offset-axicon metasurface.

with the diffractive metasurface. The positions of the metaatoms inside one supercell can be adjusted to create the needed destructive interference, while the gaps between the metaatoms are held at a constant size. With all gaps in the metasurface of the same size, any ARDE is circumvented by design. The metasurface for the two illumination modules is called an offset-axicon metagrating and is designed to produce the fan-shaped beam from the divergent Gaussian beam of a bottom-emitting VCSEL. It is referred to as a metagrating since it is the one-dimensional version of the diffractive metasurface, where the metaatoms of the supercell are grating lines that are positioned and sized to create the destructive interference needed to channel light into one desired diffraction order.

To design a metagrating that can shape the beam from the VCSEL into a fan-shaped beam, it is necessary to take another route than the conventional phase-mapping design. Instead of discretizing the desired phase profile, the metagrating is first designed for the wanted deflection angle and then formed into concentric rings, creating the phase profile of an axicon, as shown in Fig. 4.1. An axicon would form a Bessel beam if the incident beam is aligned with the center of the concentric circles. However, by moving the axicon phase profile off-center, along the x-axis in Fig. 4.1, the imparted phase profile will now be linear along the x-axis, which corresponds to deflection, and a hyperbolic profile along the x-axis, that can be used to focus light.

Since the gradient hyperbolic phase profile depends on the offset of the axicon from the center, it will decide the focusing strength of the metagrating along the y-axis. The phase profile for an axicon with an offset along the x-axis becomes

$$\phi_{\text{axicon}}(x, y) = -\frac{2\pi n_{\text{out}}}{\lambda}\text{NA}\sqrt{(x - x_0)^2 + y^2}, \tag{4.2}$$

where x_0 is the offset between the optical axis of the axicon and the reference coordinate system. The focal length that x_0 corresponds to can be found by comparing it to the phase profile for a lens, Eq. 3.2. A certain offset, x_0, will make the difference between the hyperbolic phase distribution of the offset axicon and the hyperbolic phase from the lens with a certain focal length, f, approach zero along the y-axis as

$$\begin{aligned}\Delta\phi(0, y) &= \phi_{\text{lens}}(0, y) - \phi_{\text{axicon}}(0, y) \to 0 \\ &= n_{\text{out}}\text{NA}\sqrt{x_0^2 + y^2} - n_{\text{prop}}\left(\sqrt{y^2 - f^2} - f\right) \to 0,\end{aligned} \tag{4.3}$$

where n_{prop} is the refractive index of the medium, for which the focal length is set for. Eq. 4.3 can be solved to find the needed offset x_0 to achieve a certain focal length, f, for the hyperbolic phase profile of the offset-axicon metagrating.

Since the beam from the VCSEL that is incident on the metagrating has certain divergence, characterized in Sec. 2.2.4, x_0 of the fabricated metagrating is set to counteract the spherical wavefront of the beam incident on the offset-axicon metagrating, which results in the collimation of the beam from the hyperbolic phase profile. For the linear phase profile in the other dimension, the inherent divergence of the VCSEL is maintained, which produces a broader range of angles centered around the deflection angle of the metagrating, Eq. 3.13. The fabricated offset-axicon metagratings have proven to be able to very efficiently produce the fan-shaped beam into both an air, $\eta_{\text{rel}} > 86\%$, and a glass, $\eta_{\text{rel}} > 71\%$, environment. The large efficiency is attributed to the high fidelity fabrication enabled by the elimination of the ARDE, and the high-quality material provided by the epitaxially grown GaAs.

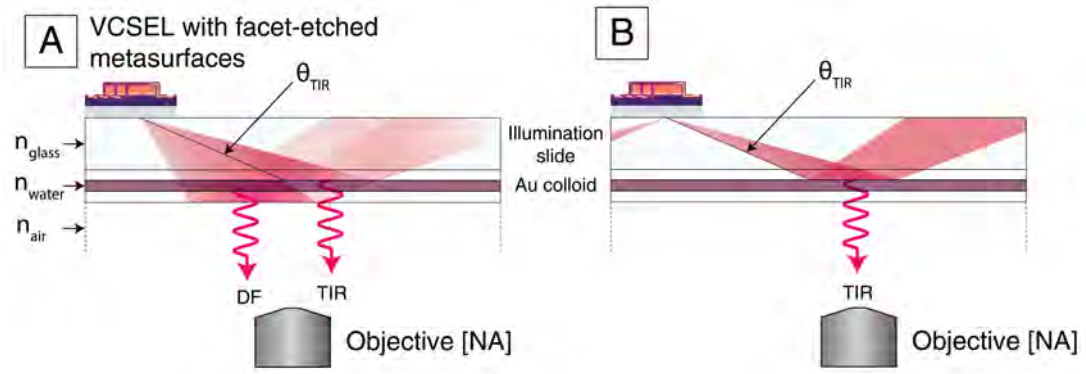

Figure 4.2: (**A**) The VCSEL with the full offset-axicon metagrating that produces a combined DF and TIR illumination. (**B**) The neighboring VCSEL with the divided offset-axicon metagrating that only produces TIR illumination.

4.3 Dark-field and total internal reflection microscopy

Traditionally, both DF and TIR illumination are achieved using bulky prisms or expensive high NA objectives to limit the field of view. Both techniques aim to eliminate direct light from the illumination source, which leads to a huge improvement in the signal-to-noise ratio of the images. In DF microscopy, the illumination path is partially blocked to only allow for light with angles larger than the numerical aperture of the imaging objective to illuminate the object. Thus, the collected image by the objective will only consist of the light that has been scattered from the illuminated object. In TIR microscopy, a sample is illuminated by light that is strictly above the critical angle of an interface. But since the evanescent field, as mentioned above, extends beyond the interface, light will scatter from a sample that is in close proximity to the interface. A VCSEL with an integrated offset-axicon metagrating, as described above, can be used to directly emit the beam needed for both TIR and DF microscopy. The offset-axicon metagrating was optimized for emission into a glass environment, $n_{\text{glass}} = 1.51$, with a deflection angle centered around $\theta_{\text{TIR}} = 63°$ with the diffractive period of the supercell, $a_{\text{d}} = 730$ nm. θ_{TIR} is just above the critical angle for a glass-water interface, $\theta_{\text{c}} = 62.0°$.

For a combined DF and TIR illumination, the VCSELs with offset-axicon metagrating were then bonded on a standard 1 mm thick microscopy slide and used to illuminate a microfluidic cell containing a colloidal solution

of Au nanorods, as seen in Fig. 4.2**A**. The illumination angles from the offset axicon metagrating are by design centered at 63°, but span in the range of 30°–90°. The scattering from the colloidal solution can be imaged by DF within the area that covers the angular range below the critical angle, and the nanorods that are close to the surface with TIR, within the area of light that is above the critical angle. Unfortunately, the TIR image is contaminated by the scattering from the DF illumination of the colloidal solution, which results in the combined DF and TIR illumination.

To be able to separate the TIR illumination, a second type of metagrating was fabricated, where the offset-axicon is divided into two mirror-symmetric halves that both only emit light at angles starting from 63°, strictly above the critical angle of the glass-water interface, which can be seen in Fig. 4.2**B**. The two counterpropagating beams can be used to only illuminate within TIR. The final demonstration was to fabricate chips with both lasers for the combined DF and TIR illumination and lasers with the strictly TIR illumination. With the two different types of metagrating integrated lasers adjacent on the same chip, it was possible to illuminate the same area with the two different modes of illumination and very rapidly switch between them.

4.4 Surface-plasmon resonance sensing

The same offset-axicon metagrating as in Paper **A** has been repurposed to enable a planar and miniaturized excitation module for surface plasmon polariton (SPP) excitation. Light propagates as a wave in free space by the coupling between the electric and magnetic fields. Since the electron distribution in a metal also couples to the electric field, it is possible to have propagating waves bound to the metal interface, called surface-plasmon polaritons. To excite the SPP along the metal interface, momentum matching is required between the incident beam and the surface mode. But the momentum of the SPP lies beyond the light cone in any medium. Additional in-plane momentum is needed to be supplied to the incident beam, most commonly performed with what is known as the Kretschmann configuration. For the Kretschmann configuration, a prism, with a large refractive index, is brought in contact with the metal interface and illuminated by light at a large angle. The combination of the larger refractive index and angle supplies the extra

momentum needed to excite the SPP. All attempts at miniaturization of angle-resolved SPR sensing utilize the Kretschmann configuration, and therefore rely on a bulky coupling prism to achieve the SPP excitation. The VCSEL with the offset-axicon metagrating can directly emit a beam into a glass environment with the needed momentum for SPP excitation, enabling the construction of a miniaturized and planar sensor.

By exciting the SPP in a thin metal film, usually 50 nm of Au, the evanescent field extends beyond the metal, which makes the momentum needed to excite the SPP sensitive to the refractive index within the evanescent field as

$$\sin\theta_{\mathrm{SPR}} = \frac{1}{n_{\mathrm{sub}}}\sqrt{\frac{|\varepsilon_{\mathrm{metal}}|n_{\mathrm{s}}^2}{|\varepsilon_{\mathrm{metal}}| - n_{\mathrm{s}}^2}}, \tag{4.4}$$

where θ_{SPR} is the angle needed to excite the SPP, n_{sub} is the refractive index of the glass substrate above the metal film, $\varepsilon_{\mathrm{metal}}$ is the permittivity of the metal film, and n_{s} is the sensed refractive index on the metal surface. Measuring the change of the coupling condition due to refractive index changes is called surface plasmon resonance (SPR) sensing. In Fig. 4.3**A** a simulated resonance spectrum can be seen, with water as the analyte, $n_{\mathrm{s}} = 1.333$, and the drift of the dip as n_{s} is increased. For our sensor, with a planar geometry, the angle of the SPP excitation is projected as

$$x = 2t_{\mathrm{glass}}\tan(\theta_{\mathrm{SPR}}), \tag{4.5}$$

where t_{glass} is the thickness of the glass slide that the VCSEL are bonded to.

A cross-section of the miniaturized SPR sensor can be seen in Fig. 4.3**B**. The array of VCSELs with facet-etched metagratings is bonded using an index-matched optical adhesive on a 1.0 mm thick glass slide with patterned contact tracks for wire bonding. Additionally, because the angle for SPP excitation lies beyond the critical angle, light will be internally reflected at the top glass surface. To be able to couple the information-carrying light from the chip, Au lines with the width 2 μm and spaced by 15 μm are patterned to the top glass surface. The thin Au lines scatter out the field intensity at discrete points. Finally, the sensor chip with the thin film that supports SPP excitation is a 0.4 mm thick glass slide with patterned 5/50 nm Ti/Au strips. The dimensions of the strips are 600x6000 μm, and aligned with the VCSEL illumination. The sensor

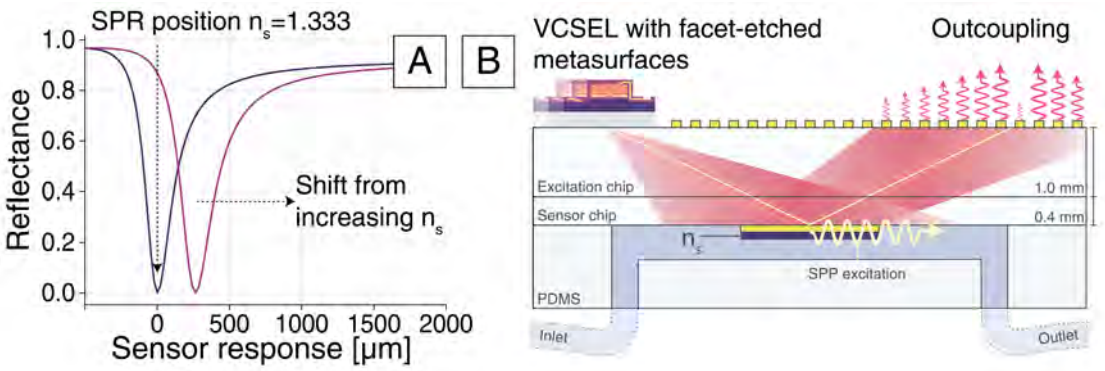

Figure 4.3: (**A**) Simulated SPR dip in reflectance that changes position with the refractive index changes of n_s within the evanescent field. (**B**) A cross-section of the miniaturized and planar SPR biosensor.

chip is bonded together with microfluidic channels on the other side for analyte perfusion. The microfluidics are fabricated in PDMS by etching a Si master mold with deep reactive ion etching and then molding the microfluidics into a PDMS slab. The microfluidic layout has three channels with equal lengths, equal numbers of bends, and with an individual inlet and outlet for each channel. This design ensures equal hydraulic resistance for all three sensing channels.

CHAPTER 5

Future work

The future work is to continue the path with miniaturized biophotonics. A new type of diffractive metasurface has been designed, and the prototype holds some promise to extend the successful offset-axicon metagrating concept into two dimensions. Since the metagrating is still based on grating lines, it is impossible to fully focus a linearly polarized beam. By taking the same concept but extending it into one more dimension, by etching holes instead, it should be possible to focus the beam from a VCSEL with a very high NA. Which could be used to construct miniaturized optical tweezers. Secondly, one noise source in the SPR sensor is the fact that light is waveguided by total internal reflection in the glass slide to which the VCSEL is bonded. The waveguided mode also has an evanescent field that extends beyond the interface and has a possibility to be utilized for another miniaturized biosensing module.

CHAPTER 6

Summary of papers

Paper A
High-angle deflection of metagrating-integrated laser emission for high-contrast microscopy
Nature: Light Science and Applications, October 13, 2023

In Paper **A** we demonstrate a miniaturized illumination module for dark-field and total internal reflection microscopy. Flat meta-optic components offer the potential to replace traditional optical elements, paving the way for highly compact biophotonic devices when combined with on-chip light sources and detectors. However, achieving efficient light shaping into wide angular wavefronts, crucial for high-contrast microscopy, remains challenging. In this work, we present curved GaAs metagratings integrated with vertical-cavity surface-emitting lasers (VCSELs) to enable on-chip illumination for total internal reflection and dark-field microscopy. Leveraging an innovative design that avoids aspect ratio-dependent etching issues in monolithic integration, we achieve off-axis emission at 60° in air and 63° in glass, with relative deflection efficiencies exceeding 90% and 70%, respectively. The emitted laser beam is collimated out-of-plane while maintaining Gaussian divergence in-plane, creating a long and narrow illumination region. Additionally, we demonstrate that different metagrating-integrated VCSEL configurations can be combined for rapid switching between dark-field and total internal re-

flection modes. This approach delivers a flexible and high-performance illumination solution for high-contrast imaging, compatible with conventional microscopy systems and adaptable to biophotonic applications such as portable microscopy, NIR-II bioimaging, and lab-on-a-chip devices.

Paper B
Flat Plasmonic Biosensor with an On-Chip Metagrating-Integrated Laser

Submitted.

In paper **B** we demonstrate a miniaturized biosensor module for surface plasmon resonance (SPR) sensing. Traditional SPR sensors are limited by bulky prism components, restricting their use in miniaturized applications. To overcome this, we developed an innovative SPR sensor using a metasurface-integrated vertical-cavity surface-emitting laser. This laser enables direct angle-resolved SPR sensing in a compact form, combined with a multichannel microfluidic cell for multi-analyte testing. Our device demonstrated resolution in refractive index that is comparable to the state-of-the-art and achieved direct detection of miRNA detection, highlighting its potential for point-of-care applications.

References

[1] T. H. Maiman, "Stimulated Optical Radiation in Ruby," *Nature*, vol. 187, pp. 493–494, Aug. 1960.

[2] J. Powell, *CO2 Laser Cutting*. Springer London, 1993.

[3] B. P. Abbott, "LIGO: the Laser Interferometer Gravitational-Wave Observatory," *Rep. Prog. Phys.*, vol. 72, p. 076901, July 2009.

[4] P. G. O'Shea and H. P. Freund, "Free-Electron Lasers: Status and Applications," *Science*, vol. 292, pp. 1853–1858, June 2001.

[5] L. A. Coldren, S. W. Corzine, and M. L. Mašanović, *Diode Lasers and Photonic Integrated Circuits*. Wiley, 1 ed., Mar. 2012.

[6] G. P. Agrawal and N. K. Dutta, *Semiconductor Lasers*. Springer US, 1993.

[7] F. Hjort, "A 310 nm Optically Pumped AlGaN Vertical-Cavity Surface-Emitting Laser," *ACS Photonics*, vol. 8, pp. 135–141, Jan. 2021.

[8] T. Nishibayashi, R. Kondo, E. Matsubara, R. Yamada, Y. Imoto, K. Hattori, S. Iwayama, T. Takeuchi, S. Kamiyama, H. Miyake, K. Naniwae, K. Miyoshi, A. Yamaguchi, and M. Iwaya, "Fabrication of vertical AlGaN-based ultraviolet-B laser diodes using a laser lift-off method," *Appl. Phys. Express*, vol. 16, p. 104001, Oct. 2023.

[9] S. Nakamura, "InGaN-based violet laser diodes," *Semicond. Sci. Technol.*, vol. 14, pp. R27–R40, June 1999.

[10] T. Hamaguchi, Y. Hoshina, K. Hayashi, M. Tanaka, M. Ito, M. Ohara, T. Jyoukawa, N. Kobayashi, H. Watanabe, M. Yokozeki, R. Koda, and K. Yanashima, "Room-temperature continuous-wave operation of green vertical-cavity surface-emitting lasers with a curved mirror fabricated on 20 21 semi-polar GaN," *Appl. Phys. Express*, vol. 13, p. 041002, Apr. 2020.

[11] M. Ishikawa, Y. Ohba, H. Sugawara, M. Yamamoto, and T. Nakanisi, "Room-temperature cw operation of InGaP/InGaAlP visible light laser diodes on GaAs substrates grown by metalorganic chemical vapor deposition," *Applied Physics Letters*, vol. 48, pp. 207–208, Jan. 1986.

[12] G. Hatakoshi, K. Itaya, M. Ishikawa, M. Okajima, and Y. Uematsu, "Short-wavelength InGaAlP visible laser diodes," *IEEE J. Quantum Electron.*, vol. 27, pp. 1476–1482, June 1991.

[13] Z. Wang, B. Tian, M. Pantouvaki, W. Guo, P. Absil, J. Van Campenhout, C. Merckling, and D. Van Thourhout, "Room-temperature InP distributed feedback laser array directly grown on silicon," *Nature Photon*, vol. 9, pp. 837–842, Dec. 2015.

[14] S. Sprengel, C. Grasse, P. Wiecha, A. Andrejew, T. Gruendl, G. Boehm, R. Meyer, and M. Amann, "InP-Based Type-II Quantum-Well Lasers and LEDs," *IEEE J. Select. Topics Quantum Electron.*, vol. 19, pp. 1900909–1900909, July 2013.

[15] J. Faist, F. Capasso, D. L. Sivco, C. Sirtori, A. L. Hutchinson, and A. Y. Cho, "Quantum Cascade Laser," *Science*, vol. 264, pp. 553–556, Apr. 1994.

[16] K. Shigihara, Y. Nagai, S. Karakida, A. Takami, Y. Kokubo, H. Matsubara, and S. Kakimoto, "High-power operation of broad-area laser diodes with GaAs and AlGaAs single quantum wells for Nd:YAG laser pumping," *IEEE J. Quantum Electron.*, vol. 27, pp. 1537–1543, June 1991.

[17] P. Lacovara, H. K. Choi, C. A. Wang, R. L. Aggarwal, and T. Y. Fan, "Room-temperature diode-pumped Yb:YAG laser," *Opt. Lett.*, vol. 16, p. 1089, July 1991.

[18] A. Oosenbrug, "Reliability aspects of 980-nm pump lasers in EDFA applications," p. 20, Apr. 1998.

[19] R. Dingle, C. Weisbuch, H. L. Störmer, H. Morkoç, and A. Y. Cho, "Characterization of high purity GaAs grown by molecular beam epitaxy," *Applied Physics Letters*, vol. 40, pp. 507–510, Mar. 1982.

[20] M. Heiblum, E. E. Mendez, and L. Osterling, "Growth by molecular beam epitaxy and characterization of high purity GaAs and AlGaAs," *Journal of Applied Physics*, vol. 54, pp. 6982–6988, Dec. 1983.

[21] H. Temkin and J. C. M. Hwang, "Undoped, semi-insulating GaAs layers grown by molecular beam epitaxy," *Applied Physics Letters*, vol. 42, pp. 178–180, Jan. 1983.

[22] P. N. Uppal and H. Kroemer, "Molecular beam epitaxial growth of GaAs on Si(211)," *Journal of Applied Physics*, vol. 58, pp. 2195–2203, Sept. 1985.

[23] H. Soda, K.-i. Iga, C. Kitahara, and Y. Suematsu, "GaInAsP/InP Surface Emitting Injection Lasers," *Jpn. J. Appl. Phys.*, vol. 18, pp. 2329–2330, Dec. 1979.

[24] P. Westbergh, R. Safaisini, E. Haglund, J. S. Gustavsson, A. Larsson, M. Geen, R. Lawrence, and A. Joel, "High-Speed Oxide Confined 850-nm VCSELs Operating Error-Free at 40 Gb/s up to 85$^{\circ}{\rm C}$," *IEEE Photon. Technol. Lett.*, vol. 25, pp. 768–771, Apr. 2013.

[25] D. M. Kuchta, A. V. Rylyakov, C. L. Schow, J. E. Proesel, C. W. Baks, P. Westbergh, J. S. Gustavsson, and A. Larsson, "A 50 Gb/s NRZ Modulated 850 nm VCSEL Transmitter Operating Error Free to 90 °C," *J. Lightwave Technol.*, vol. 33, pp. 802–810, Feb. 2015.

[26] J. Geske, C. Wang, M. MacDougal, R. Stahl, D. Follman, H. Garrett, T. Meyrath, D. Snyder, E. Golden, J. Wagener, and J. Foley, "High power VCSELs for miniature optical sensors," p. 76150E, Feb. 2010.

[27] M. Grabherr, H. Moench, and A. Pruijmboom, "VCSELs for Optical Mice and Sensing," in *VCSELs* (R. Michalzik, ed.), vol. 166, pp. 521–538, Springer Berlin Heidelberg, 2013. Series Title: Springer Series in Optical Sciences.

[28] K. Miyamoto, "The Phase Fresnel Lens," *J. Opt. Soc. Am.*, vol. 51, p. 17, Jan. 1961.

[29] J. Elton, "A Light to Lighten our Darkness: Lighthouse Optics and the Later Development of Fresnel's Revolutionary Refracting Lens 1780–1900," *The International Journal for the History of Engineering & Technology*, vol. 79, pp. 183–244, July 2009.

[30] G. J. Swanson, "Binary Optics Technology: The Theory and Design of Multi-Level Diffractive Optical Elements:," tech. rep., Defense Technical Information Center, Aug. 1989.

[31] S. N. Khonina, N. L. Kazanskiy, R. V. Skidanov, and M. A. Butt, "Advancements and Applications of Diffractive Optical Elements in Contemporary Optics: A Comprehensive Overview," *Adv Materials Technologies*, p. 2401028, Aug. 2024.

[32] I. Minin and O. Minin, *Diffractive Optics and Nanophotonics: Resolution Below the Diffraction Limit*. SpringerBriefs in Physics, Springer International Publishing, 2016.

[33] H.-T. Chen, A. J. Taylor, and N. Yu, "A review of metasurfaces: physics and applications," *Rep. Prog. Phys.*, vol. 79, p. 076401, July 2016.

[34] S. M. Kamali, E. Arbabi, A. Arbabi, and A. Faraon, "A review of dielectric optical metasurfaces for wavefront control," *Nanophotonics*, vol. 7, pp. 1041–1068, June 2018.

[35] N. A. Rubin, G. D'Aversa, P. Chevalier, Z. Shi, W. T. Chen, and F. Capasso, "Matrix Fourier optics enables a compact full-Stokes polarization camera," *Science*, vol. 365, p. eaax1839, July 2019.

[36] Q. Fan, W. Xu, X. Hu, W. Zhu, T. Yue, F. Yan, P. Lin, L. Chen, J. Song, H. J. Lezec, A. Agrawal, Y. Lu, and T. Xu, "Disordered metasurface enabled single-shot full-Stokes polarization imaging leveraging weak dichroism," *Nat Commun*, vol. 14, p. 7180, Nov. 2023.

[37] N. Yu, P. Genevet, M. A. Kats, F. Aieta, J.-P. Tetienne, F. Capasso, and Z. Gaburro, "Light Propagation with Phase Discontinuities: Generalized Laws of Reflection and Refraction," *Science*, vol. 334, pp. 333–337, Oct. 2011.

[38] P. R. West, J. L. Stewart, A. V. Kildishev, V. M. Shalaev, V. V. Shkunov, F. Strohkendl, Y. A. Zakharenkov, R. K. Dodds, and R. Byren, "All-dielectric subwavelength metasurface focusing lens," *Opt. Express*, vol. 22, p. 26212, Oct. 2014.

[39] Z. Wang, T. Li, A. Soman, D. Mao, T. Kananen, and T. Gu, "On-chip wavefront shaping with dielectric metasurface," *Nat Commun*, vol. 10, p. 3547, Aug. 2019.

[40] S. Gao, C. Park, S. Lee, and D. Choi, "A Highly Efficient Bifunctional Dielectric Metasurface Enabling Polarization-Tuned Focusing and Deflection for Visible Light," *Advanced Optical Materials*, vol. 7, p. 1801337, May 2019.

[41] Y. Hu, X. Wang, X. Luo, X. Ou, L. Li, Y. Chen, Ping Yang, S. Wang, and H. Duan, "All-dielectric metasurfaces for polarization manipulation: principles and emerging applications," *Nanophotonics*, vol. 9, pp. 3755–3780, Sept. 2020.

[42] S. Chen, W. Liu, Z. Li, H. Cheng, and J. Tian, "Metasurface-Empowered Optical Multiplexing and Multifunction," *Advanced Materials*, vol. 32, p. 1805912, Jan. 2020.

[43] R. Paniagua-Domínguez, Y. F. Yu, E. Khaidarov, S. Choi, V. Leong, R. M. Bakker, X. Liang, Y. H. Fu, V. Valuckas, L. A. Krivitsky, and A. I. Kuznetsov, "A Metalens with a Near-Unity Numerical Aperture," *Nano Lett.*, vol. 18, pp. 2124–2132, Mar. 2018.

[44] R. C. Devlin, M. Khorasaninejad, W. T. Chen, J. Oh, and F. Capasso, "Broadband high-efficiency dielectric metasurfaces for the visible spectrum," *Proc. Natl. Acad. Sci. U.S.A.*, vol. 113, pp. 10473–10478, Sept. 2016.

[45] D. K. Oh, T. Lee, B. Ko, T. Badloe, J. G. Ok, and J. Rho, "Nanoimprint lithography for high-throughput fabrication of metasurfaces," *Front. Optoelectron.*, vol. 14, pp. 229–251, June 2021.

[46] M. L. Fajri, N. Kossowski, I. Bouanane, F. Bedu, P. Poungsripong, R. Juliano-Martins, C. Majorel, O. Margeat, J. Le Rouzo, P. Genevet, and B. Sciacca, "Designer Metasurfaces via Nanocube Assembly at the Air–Water Interface," *ACS Nano*, p. acsnano.4c06022, Aug. 2024.

[47] J. Sisler, P. Thureja, M. Y. Grajower, R. Sokhoyan, I. Huang, and H. A. Atwater, "Electrically tunable space–time metasurfaces at optical frequencies," *Nat. Nanotechnol.*, vol. 19, pp. 1491–1498, Oct. 2024.

[48] E. Klopfer, H. C. Delgado, S. Dagli, M. Lawrence, and J. A. Dionne, "A thermally controlled high-Q metasurface lens," *Applied Physics Letters*, vol. 122, p. 221701, May 2023.

[49] S.-Q. Li, X. Xu, R. Maruthiyodan Veetil, V. Valuckas, R. Paniagua-Domínguez, and A. I. Kuznetsov, "Phase-only transmissive spatial light modulator based on tunable dielectric metasurface," *Science*, vol. 364, pp. 1087–1090, June 2019.

[50] H. Li, D. B. Phillips, X. Wang, Y.-L. D. Ho, L. Chen, X. Zhou, J. Zhu, S. Yu, and X. Cai, "Orbital angular momentum vertical-cavity surface-emitting lasers," *Optica*, vol. 2, p. 547, June 2015.

[51] M. S. Seghilani, M. Myara, M. Sellahi, L. Legratiet, I. Sagnes, G. Beaudoin, P. Lalanne, and A. Garnache, "Vortex Laser based on III-V semiconductor metasurface: direct generation of coherent Laguerre-Gauss modes carrying controlled orbital angular momentum," *Sci Rep*, vol. 6, p. 38156, Dec. 2016.

[52] Y.-Y. Xie, P.-N. Ni, Q.-H. Wang, Q. Kan, G. Briere, P.-P. Chen, Z.-Z. Zhao, A. Delga, H.-R. Ren, H.-D. Chen, C. Xu, and P. Genevet, "Metasurface-integrated vertical cavity surface-emitting lasers for programmable directional lasing emissions," *Nat. Nanotechnol.*, vol. 15, pp. 125–130, Feb. 2020.

[53] Q. Wang, P. Ni, Y. Xie, Q. Kan, P. Chen, P. Fu, J. Deng, T. Jin, H. Chen, H. W. H. Lee, C. Xu, and P. Genevet, "On-Chip Generation of Structured Light Based on Metasurface Optoelectronic Integration," *Laser & Photonics Reviews*, vol. 15, p. 2000385, Mar. 2021.

[54] P.-N. Ni, P. Fu, P.-P. Chen, C. Xu, Y.-Y. Xie, and P. Genevet, "Spin-decoupling of vertical cavity surface-emitting lasers with complete phase modulation using on-chip integrated Jones matrix metasurfaces," *Nat Commun*, vol. 13, p. 7795, Dec. 2022.

[55] P. Fu, P. Ni, B. Wu, X. Pei, Q. Wang, P. Chen, C. Xu, Q. Kan, W. Chu, and Y. Xie, "Metasurface Enabled On-Chip Generation

and Manipulation of Vector Beams from Vertical Cavity Surface-Emitting Lasers," *Advanced Materials*, vol. 35, p. 2204286, Mar. 2023.

[56] D. Wen, J. Meng, J. J. Cadusch, and K. B. Crozier, "VCSELs with On-Facet Metasurfaces for Polarization State Generation and Detection," *Advanced Optical Materials*, vol. 9, p. 2001780, May 2021.

[57] X. Jia, J. Kapraun, J. Wang, J. Qi, Y. Ji, and C. Chang-Hasnain, "Metasurface reflector enables room-temperature circularly polarized emission from VCSEL," *Optica*, vol. 10, p. 1093, Aug. 2023.

[58] M. Juodėnas, E. Strandberg, A. Grabowski, J. Gustavsson, H. Šípová Jungová, A. Larsson, and M. Käll, "High-angle deflection of metagrating-integrated laser emission for high-contrast microscopy," *Light Sci Appl*, vol. 12, p. 251, Oct. 2023.

[59] T. Numai, "Fundamentals of Semiconductor Lasers," in *Fundamentals of Semiconductor Lasers*, vol. 93, pp. 89–186, Springer Japan, 2015. Series Title: Springer Series in Optical Sciences.

[60] P. S. Zory, *Quantum well lasers*. Quantum electronics–principles and applications, Academic Press, 1993.

[61] N. Holonyak, R. Kolbas, R. Dupuis, and P. Dapkus, "Quantum-well heterostructure lasers," *IEEE J. Quantum Electron.*, vol. 16, pp. 170–186, Feb. 1980.

[62] E. O'Reilly and A. Adams, "Band-structure engineering in strained semiconductor lasers," *IEEE J. Quantum Electron.*, vol. 30, pp. 366–379, Feb. 1994.

[63] H. D. Kaimre, A. Grabowski, J. Gustavsson, and A. Larsson, "25 Gbaud VCSEL with Reduced Temperature Dependence," in *2024 IEEE 29th International Semiconductor Laser Conference (ISLC)*, pp. 1–2, IEEE, Sept. 2024.

[64] Y. Xiao, J. Wang, H. Liu, P. Miao, Y. Gou, Z. Zhang, G. Deng, and S. Zhou, "Multi-junction cascaded vertical-cavity surface-emitting laser with a high power conversion efficiency of 74%," *Light Sci Appl*, vol. 13, p. 60, Feb. 2024.

[65] B. E. A. Saleh and M. C. Teich, *Fundamentals of Photonics*. Wiley, 1 ed., Aug. 1991.

[66] L. Persson, "Athermalization of the Lasing Wavelength in Vertical-Cavity Surface-Emitting Lasers," *Laser & Photonics Reviews*, vol. 17, p. 2300009, Aug. 2023.

[67] K. Iga, "Surface-emitting laser-its birth and generation of new optoelectronics field," *IEEE J. Select. Topics Quantum Electron.*, vol. 6, pp. 1201–1215, Nov. 2000.

[68] E. Garmire, H. Stoll, A. Yariv, and R. Hunsperger, "Optical waveguiding in proton-implanted GaAs," *Applied Physics Letters*, vol. 21, pp. 87–88, Aug. 1972.

[69] E. Zeeb, B. Moller, C. Reiner, M. Ries, T. Hackbarth, and K. Ebeling, "Planar proton implanted VCSEL's and fiber-coupled 2-D VCSEL arrays," *IEEE J. Select. Topics Quantum Electron.*, vol. 1, pp. 616–623, June 1995.

[70] J. M. Dallesasse, N. Holonyak, A. R. Sugg, T. A. Richard, and N. El-Zein, "Hydrolyzation oxidation of AlGaAs-AlAs-GaAs quantum well heterostructures and superlattices," *Applied Physics Letters*, vol. 57, pp. 2844–2846, Dec. 1990.

[71] B. Weigl, M. Grabherr, C. Jung, R. Jager, G. Reiner, R. Michalzik, D. Sowada, and K. Ebeling, "High-performance oxide-confined GaAs VCSELs," *IEEE J. Select. Topics Quantum Electron.*, vol. 3, pp. 409–415, Apr. 1997.

[72] E. Haglund, P. Westbergh, J. S. Gustavsson, E. P. Haglund, and A. Larsson, "High-Speed VCSELs With Strong Confinement of Optical Fields and Carriers," *J. Lightwave Technol.*, vol. 34, pp. 269–277, Jan. 2016.

[73] K. D. Choquette, W. W. Chow, G. R. Hadley, H. Q. Hou, and K. M. Geib, "Scalability of small-aperture selectively oxidized vertical cavity lasers," *Applied Physics Letters*, vol. 70, pp. 823–825, Feb. 1997.

[74] K. Choquette, K. Geib, C. Ashby, R. Twesten, O. Blum, H. Hou, D. Follstaedt, B. Hammons, D. Mathes, and R. Hull, "Advances in selective wet oxidation of AlGaAs alloys," *IEEE J. Select. Topics Quantum Electron.*, vol. 3, pp. 916–926, June 1997.

[75] G. R. Hadley, "Effective index model for vertical-cavity surface-emitting lasers," *Opt. Lett.*, vol. 20, p. 1483, July 1995.

[76] J. S. Gustavsson, "Efficient and individually controllable mechanisms for mode and polarization selection in VCSELs, based on a common, localized, sub-wavelength surface grating," *Opt. Express*, vol. 13, no. 17, p. 6626, 2005.

[77] A. Haglund, "Design and Evaluation of Fundamental-Mode and Polarization-Stabilized VCSELs With a Subwavelength Surface Grating," *IEEE J. Quantum Electron.*, vol. 42, pp. 231–240, Mar. 2006.

[78] E. Hecht, *Optics*. Pearson, 5 ed/fifth edition, global edition ed., 2017.

[79] L. J. Sargent, J. M. Rorison, M. Kuball, R. V. Penty, I. H. White, S. W. Corzine, M. R. T. Tan, S. Y. Wang, and P. J. Heard, "Investigation of polarization-pinning mechanism in deep-line-etched vertical-cavity surface-emitting lasers," *Applied Physics Letters*, vol. 76, pp. 400–402, Jan. 2000.

[80] D. Lei, D.-H. Kim, N. Babazadeh, D. T. D. Childs, and R. A. Hogg, "Polarization-pinning in substrate emission multi-mode vertical-cavity surface-emitting lasers using deep trenches," *Applied Physics Letters*, vol. 120, p. 211102, May 2022.

[81] G. Hadley, K. Lear, M. Warren, K. Choquette, J. Scott, and S. Corzine, "Comprehensive numerical modeling of vertical-cavity surface-emitting lasers," *IEEE J. Quantum Electron.*, vol. 32, pp. 607–616, Apr. 1996.

[82] N. Kundtz and D. R. Smith, "Extreme-angle broadband metamaterial lens," *Nature Mater*, vol. 9, pp. 129–132, Feb. 2010.

[83] T. J. Cui, R. Liu, and D. Smith, *Metamaterials: Theory, Design, and Applications*. SpringerLink Bücher, Springer US, 2010.

[84] A. I. Kuznetsov, A. E. Miroshnichenko, M. L. Brongersma, Y. S. Kivshar, and B. Luk'yanchuk, "Optically resonant dielectric nanostructures," *Science*, vol. 354, p. aag2472, Nov. 2016.

[85] G. Zheng, H. Mühlenbernd, M. Kenney, G. Li, T. Zentgraf, and S. Zhang, "Metasurface holograms reaching 80% efficiency," *Nature Nanotech*, vol. 10, pp. 308–312, Apr. 2015.

[86] Z. Zalevsky, R. G. Dorsch, and D. Mendlovic, "Gerchberg–Saxton algorithm applied in the fractional Fourier or the Fresnel domain," *Opt. Lett.*, vol. 21, p. 842, June 1996.

[87] S. Pancharatnam, "Generalized theory of interference, and its applications: Part I. Coherent pencils," *Proc. Indian Acad. Sci.*, vol. 44, pp. 247–262, Nov. 1956.

[88] M. Berry, "The Adiabatic Phase and Pancharatnam's Phase for Polarized Light," *Journal of Modern Optics*, vol. 34, pp. 1401–1407, Nov. 1987.

[89] Y. Ra'di, D. L. Sounas, and A. Alù, "Metagratings: Beyond the Limits of Graded Metasurfaces for Wave Front Control," *Phys. Rev. Lett.*, vol. 119, p. 067404, Aug. 2017.

[90] T. Gahlmann and P. Tassin, "Deep neural networks for the prediction of the optical properties and the free-form inverse design of metamaterials," *Phys. Rev. B*, vol. 106, p. 085408, Aug. 2022.

[91] R. Yuste, "Fluorescence microscopy today," *Nat Methods*, vol. 2, pp. 902–904, Dec. 2005.

[92] Y. M. Sigal, R. Zhou, and X. Zhuang, "Visualizing and discovering cellular structures with super-resolution microscopy," *Science*, vol. 361, pp. 880–887, Aug. 2018.

[93] D. Huang, E. A. Swanson, C. P. Lin, J. S. Schuman, W. G. Stinson, W. Chang, M. R. Hee, T. Flotte, K. Gregory, C. A. Puliafito, and J. G. Fujimoto, "Optical Coherence Tomography," *Science*, vol. 254, pp. 1178–1181, Nov. 1991.

[94] A. Ashkin, "Optical trapping and manipulation of neutral particles using lasers," *Proc. Natl. Acad. Sci. U.S.A.*, vol. 94, pp. 4853–4860, May 1997.

[95] P. N. Prasad, *Introduction to biophotonics*. Wiley-Interscience, 2003.